JGR Atmospheres

RESEARCH ARTICLE
10.1029/2019JD031625

Key Points:
- Remote sensing observations of Icelandic eruptions distinguish different types of volcanic emissions
- Evidence of downwind aerosol formation, particle hydration, and possible activation were identified in Icelandic plumes
- Variations in derived particle proxies in ash-rich plumes correlate with changes in eruptive processes and magma composition

Supporting Information:
- Table S1
- Table S2
- Table S3
- Table S4
- Table S5
- Table S6
- Table S7
- Figure S1
- Figure S2

Correspondence to:
V. J. B. Flower,
verity.j.flower@nasa.gov

Citation:
Flower, V. J. B., & Kahn, R. A. (2020). The evolution of Icelandic volcano emissions, as observed from space in the era of NASA's Earth Observing System (EOS). *Journal of Geophysical Research: Atmospheres*, *125*, e2019JD031625. https://doi.org/10.1029/2019JD031625

Received 11 SEP 2019
Accepted 27 AUG 2020
Accepted article online 9 SEPT 2020

The Evolution of Icelandic Volcano Emissions, as Observed From Space in the Era of NASA's Earth Observing System (EOS)

Verity J. B. Flower[1,2] **and Ralph A. Kahn**[1]

[1]Climate and Radiation Laboratory, Earth Science Division, NASA Goddard Space Flight Center, Greenbelt, MD, USA, [2]Universities Space Research Association, Columbia, MD, USA

Abstract Volcanoes are natural phenomena that have global environmental impacts. Satellite remote sensing can help classify volcanic eruptions and track the dispersion of emissions. We assess multiple volcanic eruptions in Iceland (Eyjafjallajökull 2010, Grímsvötn 2011, and Holuhraun 2014–2015), using space-borne observations to infer information about the geological dynamics of each volcano and the properties and evolution of plume particles. We derive qualitative constraints on plume particle size, shape, and light-absorption characteristics from Multiangle Imaging SpectroRadiometer (MISR) space-borne imagery. With the MISR Research Algorithm (RA), we distinguish sulfate/water-dominated volcanic plumes from Holuhraun and ash-dominated plumes from Eyjafjallajökull and Grímsvötn, and even identify subtler changes in ash particle size and light-absorption within plumes. Additionally, plume heights are retrieved geometrically from MISR. These are combined with surface thermal anomalies from the MODerate resolution Imaging Spectroradiometer (MODIS) and SO_2 concentrations derived from the Ozone Monitoring Instrument (OMI) to synthesize eruption remote-sensing chronologies. Signals related to differences in particle properties are identified and linked to evolving magma composition at Eyjafjallajökull. The results illustrate the potential to distinguish qualitative differences in eruptive magma composition based on particle light absorption and plume profile from remote-sensing. For the sulfate-rich Holuhraun plumes, the influence of aerosol hygroscopic growth during transport is inferred from such data. Three processes appear to dominate plume evolution in Iceland: downwind aerosol formation, particle hydration, and particle deposition. This work demonstrates enhanced MISR capabilities and, more generally, remote-sensing analysis that can be applied globally, especially where suborbital volcano observations are limited or entirely absent.

1. Introduction

Satellite-based remote-sensing observations provide insight into the behavior of volcanoes globally, while minimizing inherent risk to life and equipment from the ambient heat and eruptive products. Satellite observations are acquired with minimal incremental financial expenditure, beyond the cost of the initial spacecraft deployment. The observations from NASA platforms are freely available, making them valuable resources for studying global volcanic activity. NASA currently operates instruments on multiple platforms that provide constraints on volcanic eruptive activity, including plume height and particle property constraints (Multiangle Imaging SpectroRadiometer [MISR], Cloud-Aerosol LIdar and Orthogonal Polarization [CALIOP]), gaseous emission quantification (Ozone Monitoring Instrument [OMI]), and observations of thermally radiating features (MODerate resolution Imaging Spectroradiometer [MODIS]). The longevity of platforms housing these instruments, such as Terra (>19 years), Aqua (>17 years), Aura (>15 years), and CALIPSO (>14 years), provides a significant data catalog for investigating volcanic systems. Although other instruments offering some similar capabilities are available, MISR, MODIS, and OMI data are the focus of the current work.

This study addresses the three Icelandic volcanoes that were active during the 19-year period covered by the NASA Earth Observing System (EOS) to date. Detailed discussion of the individual eruptions have previously been published for: Eyjafjallajökull 2010 (e.g., Arason et al., 2011; Cioni et al., 2014; Gudmundsson et al., 2012; Kahn & Limbacher, 2012; Sigmarsson et al., 2011; Sigmundsson et al., 2010), Grímsvötn 2011 (Moxnes et al., 2014; Petersen et al., 2012; Prata et al., 2017), and Holuhraun 2014–2015

(e.g., Ágústsdóttir et al., 2016; Gíslason et al., 2015; Pedersen et al., 2017), which we use to help validate our satellite-derived interpretations. A summary of volcanic activity during the study period is provided in Table 1.

In the current paper, we compile data from the NASA EOS space-borne MISR, MODIS, and OMI instruments and analyze the observed patterns to infer whatever information we can about the underlying geological processes occurring in Icelandic volcanic systems. Satellite-derived interpretations of volcanic processes are subsequently compared to available literature from ground-based observations to assess the validity of the deductions made. In previous work with Kamchatka Peninsula volcanic plumes, we developed many of the data analysis and interpretation processes applied here (Flower & Kahn, 2017a, 2017b, 2018, 2020). The approach is summarized in section 2, the application of which to the Icelandic volcanoes represents a test of its robustness, in a region exhibiting significant, diverse eruptive behaviors. Section 3 provides an overview of the plume and lava-flow cases captured by the satellite data. In section 4, we present our interpretations of plume and eruption dynamics derived from the satellite observations, specifically for the 2010 Eyjafjallajökull eruption, the 2014–2015 Holuhraun eruption, and the May 2011 eruption of Grímsvötn. Conclusions of this work are given in section 5.

2. Methodology

Coverage is a critical element for space-based observation of volcanic emissions, which is extensive, but can be sporadic or short-lived. The observed temporal and spatial sampling of satellite instruments depends primarily on the orbit characteristics and sensor measurement swath width, along with meteorological factors such as cloud cover. Low Earth Orbiting (LEO) satellites are the primary focus of this work, with observation frequency ranging from once every 16 days over a small fraction of the planet (CALIOP) to twice daily global coverage (MODIS). The noncontinuous observation frequencies of each instrument make a multisensor technique imperative for assessing volcanic systems comprehensively. However, for polar-orbiting instruments in general, observation frequency increases for targets at higher latitudes due to the convergence of orbits at the poles. Other factors being equal, relatively favorable coverage statistics for Icelandic volcanoes are expected.

2.1. MISR

The primary instrument of this study is the Multiangle Imaging SpectroRadiometer (MISR). It was launched aboard NASA's Terra satellite in December 1999, into a sun-synchronous orbit with day-side equator crossing at ~10:30 a.m. local time. MISR is a passive, visible-near infrared (VIS-NIR) sensor, measuring upwelling shortwave radiance in four spectral bands (446, 558, 672, and 866 nm; Diner et al., 1998). MISR provides near coincident imagery from nine cameras viewing at nadir, plus four steeper angles (26.1°, 45.6°, 60°, 70.5°) in the forward (F) and aft (A) directions, along the orbit track. Each camera views a common swath ~380 km wide, measuring at 1.1 km pixel resolution in each band. Improved resolution (275 m) is available in the nadir camera measurements and for the red spectral band in each of the other eight cameras. From MISR data, plume heights and the associted wind vectors are calculated geometrically from the multiangle imagery where there is sufficient contrast among the plume pixels (Flower & Kahn, 2017a; Kahn et al., 2007; Moroney et al., 2002; Muller et al., 2002; Nelson et al., 2008, 2013). Particle microphysical properties are derived radiometrically from the multiangle, multispectral MISR data (Martonchik et al., 2009; Kahn et al., 2010; Limbacher & Kahn, 2014, 2017; Kahn & Gaitley, 2015).

2.1.1. MISR MINX Plume-Height Retrievals

The MISR INteractive eXplorer (MINX) software was designed to retrieve plume height geometrically from multiangle imagery relatively easily, on a case-by-case basis (Nelson et al., 2008, 2013). MINX was used to analyze all the Icelandic plumes in the MISR data record for this study. It derives plume elevation from the parallax of contrast features in the plume, that is, the apparent change in the location of plume features relative to the underlying surface, as observed from varying MISR view angles (Kahn et al., 2007; Moroney et al., 2002; Muller et al., 2002; Scollo et al., 2010). This geometric technique is stable over time and independent of the radiometric calibration requirements for complimentary aerosol amount and particle-type retrievals (Flower & Kahn, 2017a; Kahn et al., 2007). The MISR red-band (672 nm) imagery was used for height determination in most cases here, due to improved horizontal spatial resolution (275 m) compared to the MISR blue band. However, when plume/surface contrast is low (e.g., over land), the blue band (446 nm)

Journal of Geophysical Research: Atmospheres 10.1029/2019JD031625

Table 1
Summary of Active Volcanoes and Eruptive Characteristics Observed in Iceland During the Analysis Period 2000–2019

Volcano[a] (location) (altitude)	Activity[a]	Magma[a] composition	Recent eruptive periods	MISR plume[b] observations	Plume heights[b] (MINX-derived averages)	MISR plume[b] particle characteristics	MODIS [OMI]
Eyjafjallajökull	Elongated, ice-covered stratovolcano generating fissure-fed lava flows	Trachyandesite, Trachyte, Rhyolite	A single eruptive event in recent historical time occurred in ***April–June 2010***	***Total plumes*** identified – 19	***Min*** – 2.2 km Mean – 3.4 km Max – 5.3 km	Composite of small, spherical, and medium, nonspherical components	***Max*** Radiance – 88 $W\ m^{-2}\ sr^{-1}\ \mu m^{-1}$ *Trend –Variable (Bimodal: somewhat increasing)*
63.63°N, 19.63°W	Prior confirmed eruption – 1821–1823	(Gudmundsson et al., 2012)		***In-depth*** investigation – 15	Trend – Variable (somewhat increasing) over time	Mixed sulfate/ash plumes.	[Daily max SO_2 – 53 kt; Trend – Unimodal: peak 8 May 2010]
1,651 m	(Gudmundsson & Hoskuldsson, 2019)						
Grímsvötn	Frequently active fissure system. Eruptions lasting days to months	Basalt	Two eruptions, predominantly active on the SW of the caldera: ***November 2004*** and ***May 2011***	***Total plumes*** in May 2011 – 3	***Min*** – 0.3 km Mean – 5.8 km Max – 15.4 km	Single eruptive plume. Multilayer displaying varying properties between altitudes.	N/A
64.42°N, 17.32°E	(Larsen & Gudmundsson, 2019)	(Larsen & Gudmundsson, 2019)		***In-depth*** investigation – 2[c]	Trend – N/A	Low-altitude drifting plume imaged on subsequent day.	***[Eruption day SO_2 –150 kt; Eruption day[c] 1 SO_2 –280 kt Trend – Unimodal: peak 8 May 2010]***
1,719 m							
Holuhraun (Bárðarbunga)	Fissure eruption originating from Bárðarbunga volcano	Basalt	Fissure eruption, emitted from the Holuhraun vent, ***August 2014–February 2015***	***Total plumes*** identified – 16	***Min*** – 1.5 km Mean – 2.9 km Max – 4.2 km	Consistently small spherical components indicative of sulfates. Variation in plume properties driven by aerosol-cloud interactions.	***Max Radiance*** – 1,250 $W\ m^{-2}\ sr^{-1}\ \mu m^{-1}$ Trend – Decreasing over time
64.63°N, 17.52°E	Prior confirmed eruption – 1910	(Hartley et al., 2018)		***In-depth*** investigation – 11	Trend – Decreasing over time		[Daily max SO 2 – 136 kt; Trend – Decreasing]
2,882 m	(Gudmundsson & Larsen, 2019)						

[a]Unless otherwise stated, information compiled from: Global volcanism program, 2013. Volcanoes of the world, v. 4.8.0. Venzke, E (ed.). Smithsonian Institution. Downloaded 7 June 2019 (https://doi.org/10.5479/si.GVP.VOTW4-2013). [b]Synthesis of analyses performed in this work. [c]Second "plume" (24 May 2011) represents downwind observation of earlier observed event (22 May 2011).

Table 2
Summary of MISR RA Particle Types and Color-Codes Linked to Each Particle Type[a]

#	Model code	r_e (μm)[b]	Particle size/shape	Code[c]
1	sph_nonabs_0.06	0.056	Very small, spherical, nonabsorbing	VsSpNab
2	sph_nonabs_0.12	0.121	Small, spherical, nonabsorbing	SmSpNab
3	sph_nonabs_0.26	0.262	Small-medium, spherical, nonabsorbing	MsSpNab
4	sph_nonabs_0.57	0.568	Medium, spherical, nonabsorbing	MeSpNab
5	sph_nonabs_1.28	1.285	Large, spherical, nonabsorbing	LaSpNab
6	sph_abs_0.12_nr_1.50_0.80_flat	0.121	Small, spherical, highly absorbing (flat)	SmSpHab(f)
7	sph_abs_0.12_nr_1.50_0.80_steep	0.121	Small, spherical, highly absorbing (steep)	SmSpHab(s)
8	sph_abs_0.12_nr_1.50_0.90_flat	0.121	Small, spherical, moderately absorbing (flat)	SmSpMab(f)
9	sph_abs_0.12_nr_1.50_0.90_steep	0.121	Small, spherical, moderately absorbing (steep)	SmSpMab(s)
10[d]	dust_grains_mode1	0.754	Medium, weakly-absorbing dust grains	MeNspWab
11[d]	spheroidal_mode2	2.4	Large, weakly-absorbing coarse dust spheroids	LaSpdWab

[a]Each model is comprised of an amalgamation of particles with a designated effective radius (r_e). Additional details are provided in the supporting information. Full model details available in Limbacher and Kahn (2014). [b]Full details of component size and single scattering albedo (SSA) across spectral band provided in a supporting information. [c]Code for each component incorporating three elements: ***Size*** – very small (Vs), small (Sm), small-medium (Ms), medium (me), large (La); ***Shape*** – Spherical (Sp), spheroid (Spd), nonspherical (Nsp); ***Absorption*** – Nonabsorbing (nab), weakly absorbing (Wab), moderately absorbing (Mab), highly absorbing (Hab); ***Spectral Absorption Profile*** – Equal ("flat") absorption in all spectral bands (f); varying ("steep") absorption across spectral bands (s). [d]Dust and spheriods optical properties from Kalashnikova et al. (2005).

imagery, at 1.1 km resolution, is used. The ~7-min time-lag between the MISR 70° forward-viewing and the 70° aft-viewing cameras at a given surface location means MINX can correct the derived plume heights for any proper motion due to local wind at plume elevation (Nelson et al., 2013). Although overlying meteorological cloud can impede plume retrievals, heights can be retrieved for plumes exceeding local cloud layers. Full details of plume heights and wind retrievals for each eruption plume are included in the supporting information.

2.1.2. MISR Research Algorithm Aerosol Property Retrievals

The MISR aerosol retrieval algorithm uses the angular-spectral distribution of scattered light to derive constraints on aerosol amount, and on particle size, shape and light-absorption properties. Where retrieval conditions permit, particles having different optical properties generate different signatures in the multiangle, multispectral data. The retrieval algorithm contains a range of candidate optical models representing particles of different sizes, light-absorption characteristics, and spherical or randomly oriented nonspherical shapes. Simulations are performed with a radiative transfer code for mixtures of up to three of these optical models, over a range of aerosol column amounts, and the algorithm compares the simulated top-of-atmosphere reflectances with MISR-observed reflectances. The retrieval identifies all mixtures that pass acceptance criteria that are based upon estimated measurement uncertainty, and the range of passing mixtures defines the retrieved aerosol amount and type constraints.

MISR Standard Aerosol (SA) retrieval algorithm runs automatically on the entire MISR data stream (Martonchik et al., 2002, 2009; Garay et al., 2020). The MISR Research Aerosol (RA) retrieval algorithm expands upon the SA in terms of general accuracy, and especially aerosol particle property constraints, but it runs manually, on a case-by-case basis (Kahn et al., 2001; Limbacher & Kahn, 2014, 2017). It offers improved spatial resolution, radiometric calibration, and surface characterization, as well as a richer set of aerosol optical models in the algorithm climatology and other improvements. MISR aerosol retrievals have been used to identify dust (Guo et al., 2013; Kalashnikova & Kahn, 2006, 2008), volcanic plumes (Kahn & Limbacher, 2012; Scollo et al., 2012; Flower & Kahn, 2018), wildfire smoke (Junghenn Noyes et al., 2020), and regional and global aerosol-type distribution (e.g., Dey & Di Girolamo, 2010; Kahn & Gaitley, 2015).

Meteorological cloud can impede MISR aerosol type retrievals, and "favorable retrieval conditions" for deriving particle microphysical properties include a minimum midvisible aerosol optical depth (AOD) of about 0.15 or 0.2, and a low surface albedo with minimal variation. As such, the best MISR RA and SA retrievals tend to be performed over water, and smoke, dust, and volcanic plumes are especially good targets for MISR particle-type retrieval, due to relatively high AOD. The current study incorporates MISR RA results, using an aerosol climatology of 774 mixture groups containing up to three of 11 components (Table 2). Although not optimized specifically for analyzing volcanic particles due to a lack of optical models for volcanic ash, the MISR RA has previously been used to distinguish ash-rich from sulfate/water-rich plumes (Flower & Kahn, 2018, 2020; Kahn & Limbacher, 2012; Scollo et al., 2012). Retrieved particle size and

light-absorption properties also have practical applications in volcanic-plume assessment. (Full particle size and absorption details are provided in Table S1).

Sulfur dioxide (SO_2), typically a component of volcanic emissions (Castleman et al., 1974), is undetectable by MISR in its gaseous form. However, SO_2 is converted in liquid phase to sulfate aerosols over hours-to-days in the ambient atmosphere (Sigurdsson et al., 2015), and this process occurs readily in volcanic plumes. MISR can detect sulfate particles within volcanic plumes, as small or medium, spherical, nonlight-absorbing components (Kahn & Limbacher, 2012; Scollo et al., 2012). In the current work, sulfates are commonly identified when small-medium, spherical, nonabsorbing components are retrieved (VsSpNab, SmSpNab, MsSpNab: see Table 2 for particle details). Pure water particles of similar size are indistinguishable from sulfates in the MISR observations, so from MISR retrievals alone, such results are denoted "sulfate/water" proxies. Further, sulfate/water components within a plume are susceptible to growth by coalescing or scavenging by ash particles as transport occurs (Sparks et al., 1997). Downwind conversion of SO_2 to sulfate, and subsequent particle processing occurring within individual plumes, has also been deduced previously from MISR RA retrievals (Flower & Kahn, 2018, 2020).

Nonspherical components in the MISR RA (MeNspWab, LaSpdWab) are usually associated with ash particles in volcanic plumes. However, nonspherical optical models in the MISR RA are limited due to a lack of available constraints on airborne ash particle shape and light-scattering properties. As a result, RA retrieved aerosol "components" capture aspects of the aggregate aerosol that are optically equivalent to the particles present (Kahn & Gaitley, 2015; Kahn & Limbacher, 2012). For example, a highly light-absorbing ash plume is typically retrieved as a mixture of nonspherical dust-grain optical analogs combined with small, spherical absorbing components (Flower & Kahn, 2020; Kahn & Limbacher, 2012). To appropriately interpret the MISR size constraint provided by the retrieved aggregate of aerosol components, we refer to the *Retrieved Effective Particle Size* (REPS) in our analysis of the data, that is, the qualitative changes in effective size of the retrieved mixture of particle types. For example, a decrease in REPS corresponds to a higher AOD fraction of small components retrieved within in the plume.

Similarly, the *Retrieved Effective Particle Absorption* (REPA) gives a qualitative indication of the aggregate retrieved-component light-absorption properties, so plumes containing more absorbing particles have a higher REPA than those comprised of nonabsorbing aerosols. As derived from MISR data, spherical *light-absorbing* aerosol components can be separated into two broad categories under favorable retrieval conditions (Chen et al., 2008; Kahn & Gaitley, 2015). Spectrally "flat" components represent aerosols having single-scattering albedo (SSA) that is relatively independent of wavelength across the visible spectrum (e.g., black carbon and some soot particle types). Spectrally "steep" particles tend to absorb more strongly at blue than at red wavelengths (e.g., brown carbon particles, most commonly emanating from wildfire and other combustion sources). For volcanic plumes, the retrieval of small, spherical, absorbing particles must be viewed as representing light-absorption in the aggregate of plume particles, rather than indicating the presence of these specific aerosol components (Kahn & Limbacher, 2012). Variations in the light-absorption profile of ash plumes observed in MISR snapshots might indicate changes in the physical properties of particles, the chemical composition of erupted magma, or chemical evolution of the particles after emission. The MISR RA output has not previously been applied to the interpretation of magma-composition evolution. Therefore, where ground and in situ sampling studies of Icelandic ash are available, we compare the reported chemical evolution with MISR RA retrievals to determine if correlated plume variations are observed.

To facilitate the intercomparison of plumes across eruptive events, and between volcanoes, two qualitative descriptors have been defined for each MISR-imaged plume. Firstly, we present the retrieved plume component fractions within color-coded "cloud" cartoons (detailed information is included in Table S3 and individual plume plots in the supporting information). These breakdowns show the dominant components retrieved for each eruption. Using the component color-codes given in Table 2, we indicate the dominant particle properties in eruption chronology figures with these summary illustrations.

The second comparative graphic is the *Whole Plume Particle Proxy*, calculated for each plume by accounting for the size, shape, absorption strength, and fraction of each component retrieved by the MISR RA. Using the derived MISR RA values, we defined the broad *angularity* of particles (None, Low, Medium, and High) by considering the fraction of nonspherical components retrieved. One of the nonspherical component

optical models is not by definition "angular," being spheroidal in shape, due to the difficulty in calculating the scattering properties of larger particles with complex facets (Kalashnikova & Kahn, 2006). The majority of nonspherical retrievals are dominated by the medium, angular "dust" analog. The exception is a low altitude, possibly remobilized, ash plume observed at Grímsvötn, dominated by very large particles for which the larger, nonspherical ellipsoid model (LaSpdWab) is retrieved. (Generally, we refer to the retrieved particles as "proxies" because we are making an interpretation when we associate, e.g., medium nonspherical particle with "ash" or spherical nonabsorbing particles with "sulfate/water.") The shading of the *Whole Plume Particle Proxy* graphics, defined as the *Absorption Factor*, is derived by combining the fraction of absorbing components (e.g., SmSpHab(f), SmSpMab(s), and MeNspWab) from the MISR RA retrieval with the intensity of the retrieved absorption defined by the Single Scattering Albedo (SSA). This is presented as a guide to varying light-absorption properties within plumes. The *Whole Plume Particle Proxy* represents a qualitative marker of varying ash concentrations and morphological changes within plumes (details of the *Whole Plume Particle Proxy* values are included in Table S3).

2.2. MODIS

Launched aboard NASA's Terra satellite with MISR, the MODerate Imaging Spectroradiometer (MODIS) is a broad-swath, visible-infrared (VIS-IR) imager providing global coverage every 1–2 days (Salomonson et al., 1989; Wright et al., 2002). The combined presence of MISR and MODIS on the Terra satellite facilitates direct data comparisons and synergistic applications. A second MODIS sensor, launched on the Aqua satellite in 2002, provides additional daily daytime and nighttime observations, about 3 hr later at the equator than the Terra overpass. MODIS was designed for a range of applications, including thermal anomaly detection (Kaufman et al., 1998); these data are generated automatically and are disseminated by the MODVOLC web-based interactive database (http://modis.higp.hawaii.edu; last accessed July 2019). The MODVOLC algorithm uses the 4 and 12 μm spectral bands to identify "significant" anomalies in near-real-time, based on whether a thermally radiating feature (4 μm: MODIS band 22; or band 21 when band 22 is saturated) exceeds a predefined threshold relative to the local background (12 μm: MODIS band 32) surface radiance (Wright et al., 2002). MODVOLC data detail the occurrence, extent, and intensity of lava flow features and, to a lesser extent, lava domes and pyroclastic flow deposits (Wright et al., 2004). MODIS thermal anomalies have been widely used to locate and track volcanic eruptions (Lyons et al., 2010; Wright, 2016; Wright et al., 2002, 2004) and to investigate cyclical processes (Flower & Carn, 2015; Murphy et al., 2013).

In addition to surface thermal anomaly detection, MODIS has also been widely used to identify volcanic plumes, to map plume horizontal extent in the visible imagery, and to determine plume elevation based on thermal infrared signatures (e.g., Watson et al., 2004; Thomas & Prata, 2011; Dubuisson et al., 2014). As such, we capitalize on the wider MODIS swath width of 2,330 km (compared to MISR's 380 km width) to assess the regional environmental setting for each plume imaged by MISR. The wider views of MODIS also provide insight into large-scale atmospheric dynamics, such as the positioning of frontal systems, that can significantly affect plume dispersion.

2.3. OMI SO_2 Observations

The Ozone Monitoring Instrument (OMI) is an ultraviolet (UV) sensor providing near-global daily coverage. OMI was launched on NASA's Aura satellite in 2004, with the primary aim of obtaining daily measurements of global ozone concentrations. OMI observations are nearly coincident with those from the Aqua/MODIS. Similarities in the spectral absorption bands of ozone and key volcanic gases, particularly sulfur dioxide (SO_2) (Krotkov et al., 2006; Krueger, 1983) make it invaluable for identifying and tracking volcanic emissions (Carn et al., 2015, 2016; Krotkov et al., 2006; McCormick et al., 2013; McCormick Kilbride et al., 2019). At launch, OMI provided the highest spatial resolution available for near-global daily volcanic SO_2 measurements (13×24 km^2 at nadir). The improved resolution led to the detection of small-moderate volcanic eruptions missed by the earlier Total Ozone Mapping Spectrometer (TOMS; 40×40 km^2 at nadir) UV instruments (Carn et al., 2013, 2016; Krotkov et al., 2006). We use OMI SO_2 mapping to validate the presence of sulfates identified by the MISR RA particle property retrievals and to provide daily tracking of volcanic SO_2 emissions and plume evolution.

Since 2008, certain rows of the OMI instrument CCD array have been affected by the OMI Row Anomaly (ORA), causing inaccuracies and blockages in the radiance measured onboard the instrument. The ORA

limits our ability to complete daily volcanic observations, with near-nadir observations most significantly influenced by the anomalies (http://projects.knmi.nl/omi/research/product/rowanomaly-background.php; Flower et al., 2016; Torres et al., 2018). The impact of the ORA in Iceland is somewhat mitigated by the convergence of satellite orbits at high latitudes, where multiple overpasses, at different viewing angles each day, reduce the detrimental impacts of the ORA. OMI data were visualized and analyzed using the OMIplot software, developed by S. Carn and made available from Vhub (https://vhub.org/resources/682; last accessed April 2019). OMIplot can isolate plume features and calculate plume mass from column concentrations, and has been used frequently to identify and characterize global volcanic activity (e.g., Carn et al., 2013; McCormick et al., 2013; Flower et al., 2016). If sulfur is injected into the stratosphere, the conversion timescale is increased, and the residence time of the volcanic sulfur in the atmosphere is prolonged. The persistence of sulfate aerosol (H_2SO_4) in the stratosphere is known to make a significant contribution to the radiation budget, both locally and globally (Lacis et al., 1992; Pollack et al., 1976). Of those volcanoes analyzed in the current work, the Grímsvötn eruption of May 2011 injected significant SO_2 into the stratosphere.

2.4. CALIPSO Observations

Despite the convergence of polar orbits at high latitudes, the CALPISO measurements that were closest to MISR for the cases studied here were still acquired at significant distances from the MISR observations, due mainly to the very narrow (~100 m) CALIPSO swath. Detailed reviews of the CALIOP data related to volcanic plumes are available in a number of studies (Carboni et al., 2016; Pavolonis et al., 2013; Winker et al., 2012). Stohl et al. (2011) used plume dispersion modeling to distinguish meteorological features from Eyjafjallajökull volcanic emissions in the CALIOP retrievals. They noted that downwind plume features were difficult to separate from water and ice clouds due to similarities in the backscatter signals. As such, further interpretation of CALIOP signals is not included in the current study.

3. Overview of Remote Sensing Observations

In this section, we summarize the aggregate of remote-sensing observations used in the subsequent analysis and interpretation, which is given in section 4.

3.1. Plumes

Four Icelandic volcanic eruptions occurred within the MISR data record between March 2000 and May 2019. The earliest eruption, at Grímsvötn in 2004, did not produce any useable observations for this work due to cloud cover, short eruption duration and limited sampling; it is thus excluded from further consideration. The diverse characteristics of the three remaining eruptions (Eyjafjallajökull 2010, Grímsvötn 2011, and Holuhraun 2014–2015) are the focus of this study (Table 1). Eruption duration and style varied dramatically among these volcanoes. The Grímsvötn eruption was of short duration, lasting only 8 days. In contrast, eruptions at Eyjafjallajökull and Holuhraun persisted for 96 and 183 days, respectively. Several factors influenced the frequency with which eruptive plumes were captured in the MISR data, including daily eruption timing relative to MISR overpass time and location, plume transport direction, and the extent of meteorological cloud cover. Due to Iceland's high latitude, MISR plume observations occurred as frequently as a day apart, though most commonly at two-day intervals. Unfortunately, the high latitude and maritime climate also produced persistent meteorological cloud. Resulting plume observation totals were: Eyjafjallajökull 19 (15) plumes, Grímsvötn 3 (2) plumes, and Holuhraun 16 (11) plumes, with the numbers in parentheses representing plumes for which we could provide full MISR RA analyses (Figure 1). In each case, where a MISR RA retrieval was not possible but a plume height was retrieved using MINX, the plume is included in the eruption timelines in gray (the MINX output is given in Figures S2–S10). At Eyjafjallajökull four plumes (Eyja2010d, Eyja2010i, Eyja2010p, and Eyja2010r) could not be analyzed using the MISR RA retrievals due to extensive meteorological cloud cover. At Holuhraun, one plume retrieval (Holu2014b) was impeded by extensive cloud cover, and a further four plumes (Holu2014m, Holu2015a, Holu2015b, and Holu2015c) could not be analyzed due to low solar illumination, which produced minimal reflected radiances that are difficult to interpret with the current algorithm.

SO_2 was observed from each eruption. Eyjafjallajökull displayed minimal SO_2 emissions during the first half of the eruption cycle, but it increased rapidly about halfway through the sequence (Figure 1a). Holuhraun was unique in Iceland, generating persistent sulfur-rich plumes with minimal ash. The corresponding SO_2

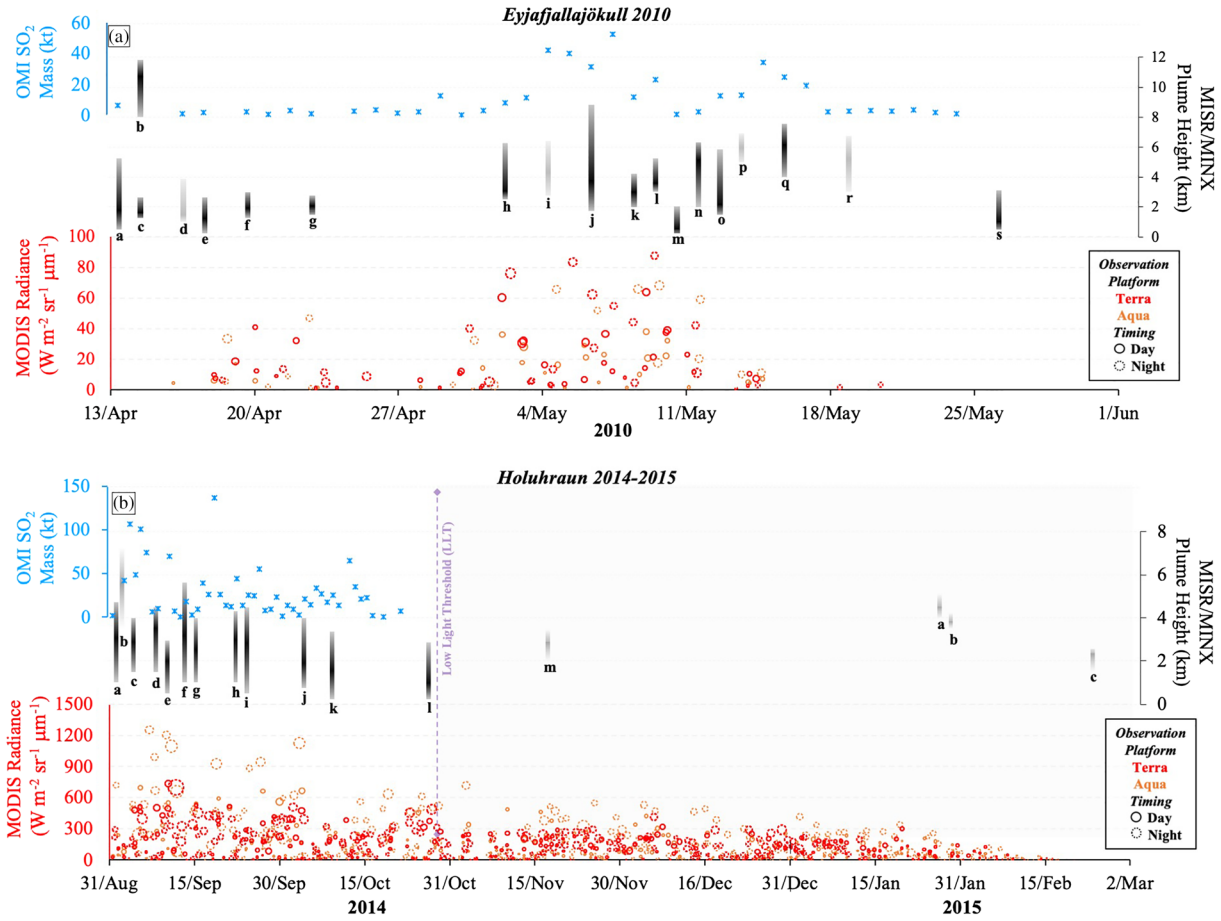

Figure 1. Timeline of multisensor observations at (a) Eyjafjallajökull 2010, and (b) Holuhraun 2014–2015. (Top row; blue axis) OMI-derived SO_2 plume mass; (middle row; black axis) MINX-derived plume heights. Plume-height retrievals indicate maximum and minimum plume extent, with the region of highest contrast represented in black. Gray height bars indicate plumes for which plume-heights were derived, but RA particle-property analysis could not be performed; (bottom row; red axis) MODIS-detected surface thermal anomalies. Note that the MODIS data point size corresponds to the daily thermal anomaly count (range: 1–8 pixels for Eyjafjallajökull; 1–210 at Holuhraun), an indication of active radiating area.

observations indicate that emissions peaked early in the eruption and gradually diminished over time (Figure 1b). Low light levels impeded the UV observations of OMI after November, preventing complete assessment of SO_2 emission for the latter two-thirds of the Holuhraun eruption. Despite the short duration of the Grímsvötn eruption, the SO_2 emissions were significant, with high column concentrations and ejection into the stratosphere.

3.2. Lava Flows

MODIS Terra and Aqua thermal anomalies, generally indictive of surface lava flows, are presented for the eruption time-series of Eyjafjallajökull and Holuhraun in Figures 1a and 1b, respectively. Thermal anomalies are shown here with the overall radiance of each day on the *y*-axis and the size of each marker representing the area of the flow for each overpass (defined by the number of radiating pixels identified by MODVOLC). Thermal anomaly counts and overall radiance at Holuhraun are considerably higher than those identified at Eyjafjallajökull due to the greater flow extent and effusion rate from the former. As thermal anomalies are assessed relative to background, diurnal and seasonal differences in ambient surface temperature can affect the magnitude of the derived anomalies (Wright et al., 2002). As such, enhanced thermal anomaly values are expected during colder times of day, and in colder seasons; the Normalized Thermal Index (NTI) of lava lakes in polar latitudes can be as much as 50% higher than identically radiating lava lakes near the equator (Wright et al., 2002).

Although no systematic difference between the Terra (Figure 1; red markers) and Aqua (Figure 1; orange markers) MODIS data appears at Eyjafjallajökull in Spring 2010 (Figure 1a), for Holuhraun in Autumn 2014, the nighttime radiant power anomaly reported by Aqua (Figure 1b; dashed orange markers) is higher than that from Terra. This is likely due to generally low ambient surface temperatures combined with differences in the satellite time-of-night sampling. The Terra satellite transits over Iceland between 21:30 and 00:00 local time (which is the same as UTC for Iceland), whereas Aqua samples later, between 03:00 and 05:30. We compared the latest nighttime observations by Terra (23:25 UTC) with the earliest from Aqua (03:25 UTC) for a single day, 4 September 2014; minimal volcano variations would be expected over the 4-hr time-difference on the ~1 km MODIS spatial scale. Yet 60% more pixels pass the MODVOLC "significant anomaly" threshold for Aqua than Terra (Terra: 19; Aqua: 33), and the values yield a higher average NTI (T: −0.326; A: −0.281). The difference between the Band 32 (~12 μm) "background" radiance (T: ~7.04; A: ~9.20 W m^{-2} sr^{-1} μm^{-1}) and Band 21/22 (both at ~4.0 μm) lava radiances (T: ~10.94; A: ~15.06 W m^{-2} sr^{-1} μm^{-1}) of the Terra and Aqua measurements were disproportionate by about 1.96 W m^{-2} sr^{-1} μm^{-1}, which shifts the passing threshold calculation in favor of the Aqua/MODIS sensor. Eight of the 33 Aqua-identified pixels were within 0.1 of the NTI threshold. This likely occurred near the flow edge, where the radiating source might not cover entire pixels. Where background values are lower, radiating areas (e.g., lava flows) smaller than the MODIS pixel area are more likely to provide enough energy to surpass the NTI threshold.

More broadly, the thermal anomaly record at Holuhraun mirrors the SO_2 observations, peaking early in the eruption and declining thereafter (Figure 1b). In contrast, the Eyjafjallajökull thermal anomaly time-series appears bimodal. The initial peak occurred ~5 days after the first MISR-imaged plume and decreased within 7 days. The second increase occurred concurrently with the MISR and OMI observations on or about 5 May 2014. Thermal detection and SO_2 emissions in the satellite record ceased on 17 May, indicating the end of the active eruption phase. The remainder of this paper presents our interpretation of the multisensor, remote-sensing volcano data.

4. Discussion—Eruption Histories and Analyses

4.1. Eyjafjallajökull, April–June 2010

A timeline of volcano remote-sensing signals and subsequent interpretations for the 2010 Eyjafjallajökull eruption is presented in Figure 2. This combines observations of MODIS thermal anomaly detection, OMI SO_2 emissions, MISR plume ejection heights (Figure 2c); MISR fractions of modeled components when the plume is considered in its entirety (Figure 2b); an illustrative representation of the plume particle size and shape when the plume particles are considered in aggregate (Figure 2a); and our interpretation of the aggregated remote-sensing observations in terms of the underlying factors driving the eruption at key points in the eruption chronology (Figure 2d), discussed in the following section. Note that the "particle size and shape" symbols are cartoons, illustrating qualitatively the relative particle size and the AOD fraction retrieved as randomly oriented nonspherical (not the actual shape, as we cannot retrieve that level of detail).

The plume particle analyses in Figure 2b represent combined whole-plume component fraction, used as a guide for assessing the evolving eruptive activity. (Full individual analysis maps for each plume in this study are provided in the supporting information.) Generally, MISR RA analyses of Eyjafjallajökull plumes were dominated by medium to large components (MeNspWab, LaSpNab, and LaSpdWab; Table 2) indicative of ash-dominated plumes. However, medium MISR RA components (MeNspWab) were observed more frequently in Iceland compared to previous analyses of Kamchatka, Russia volcanoes (Flower & Kahn, 2018, 2020). The smaller particle size generated in Icelandic eruptions is better resolved by the visual-NIR MISR measurements (maximum particle effective radius for which MISR has size-sensitivity is ~2–3 μm), which allows for improved particle size discrimination compared to eruptions producing only larger ash components. Complimentary ground-based ash sampling at Eyjafjallajökull corroborates this observation, indicating that particles were very-fine to fine in size (Cioni et al., 2014; Gudmundsson et al., 2012), in closer agreement with MeNspWab than larger components in the MISR RA (LaSpdWab, LaSpNab).

The remote sensing observations from the 2010 Eyjafjallajökull eruption can be separated into four distinct phases, and are highlighted in Figure 2: Initial emissions (Phase A; 14–17 April); Eruption lull (Phase B; 18 April to 4 May); Increased plume volatile content (Phase C; 5–18 May); and post-eruptive ash remobilization

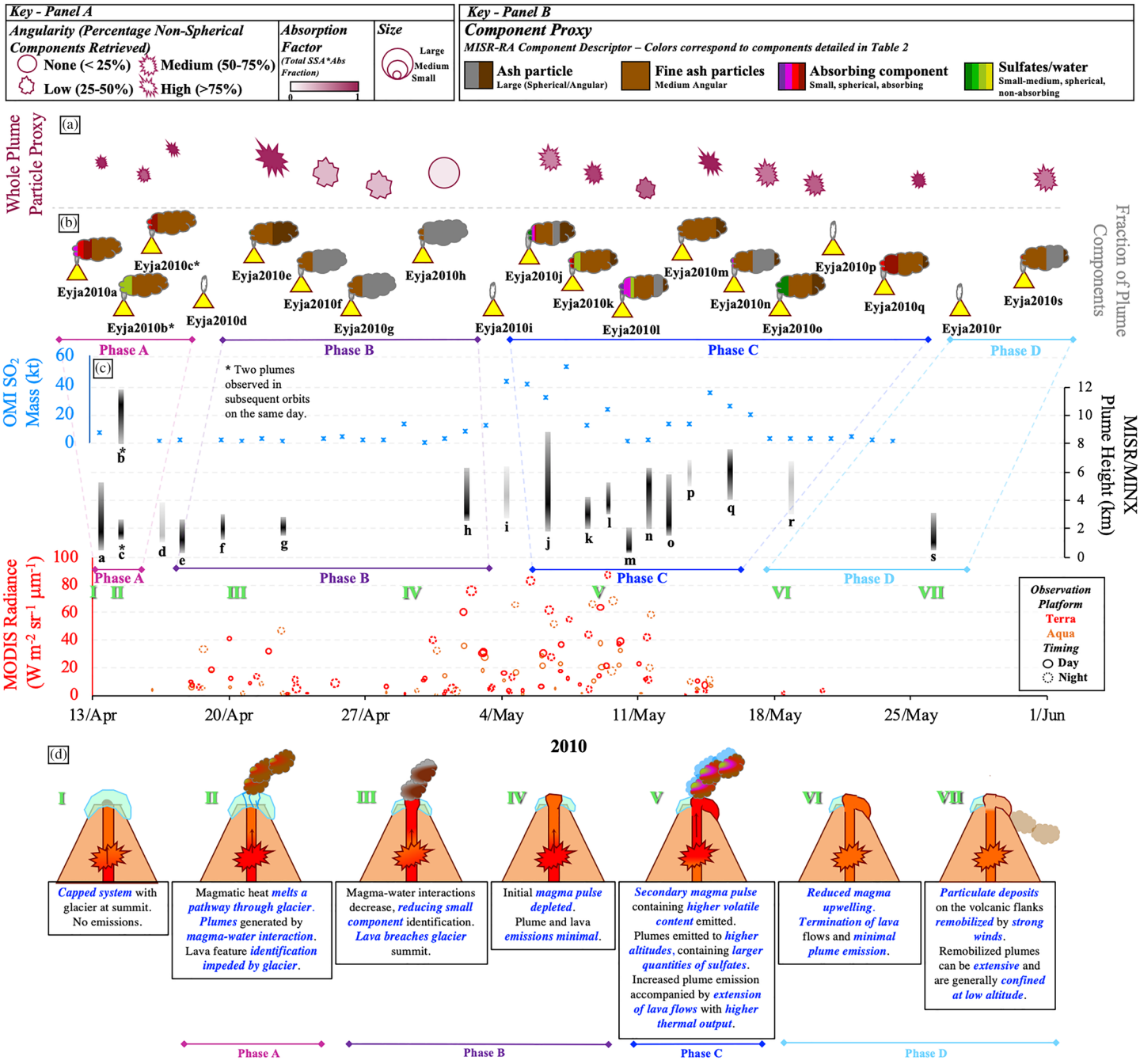

Figure 2. Timeline of Eyjafjallajökull eruption in 2010, incorporating: (a) illustrative, whole-plume particle size/shape derived from the MISR RA retrieval algorithm; (b) whole-plume particle component fraction, derived from the MISR RA retrieval algorithm (component information is given in Table 2); (c) (top row; blue axis) OMI-derived SO_2 plume mass; (middle row; black axis) MINX-derived plume heights. Retrievals indicate maximum and minimum plume extent, with the region of highest contrast represented in black. Gray height bars indicate plumes for which plume-heights were derived, but RA particle-property analysis could not be performed; (bottom row; red axis) MODIS-detected surface thermal anomalies; and (d) geological interpretation of remote sensing signals obtained from Eyjafjallajökull corresponding to points identified in panel (c). Note that MISR plume-height and OMI SO_2 data correlate to the MODIS timeline *x*-axis at the bottom of the panel (c), whereas the plume and particle-proxy cartoons are spread out for easier visibility. Colored lines at the bottom of panel (b) delineate and distinguish eruption phases and associate the cartoons with the timeline. The MODIS data-point size corresponds to the daily thermal anomaly count (range: 1–8 pixels in this case) as an indication of active radiating area. Full, individual MISR plume retrievals (MISR height, RA, and OMI data) and MODIS thermal anomaly data used to compile this figure are provided in the supporting information. Detailed analysis from which geological interpretations were derived is included in section 4.1.

(Phase D; 9–25 May). Our satellite-derived phases align well with complimentary ground-based eruption chronologies derived from tephra samples, along with plume, weather, and crater observations (Gudmundsson et al., 2012) highlighting four eruption phases: an initial explosive phase (14–18 April); a lower discharge, effusive phase (18 April to 4 May); a secondary explosive phase (5–17 May); and the final declining phase (18–22 May). A discussion of the satellite-observed signals is given in the remainder of this section, with ground-based records referenced where relevant for validation or enhanced interpretation.

4.1.1. Eruption Chronology Based on Remote Sensing Data

Phase A constitutes the initial resurgent activity period (14–17 April), after almost two centuries of quiescence (Gudmundsson & Hoskuldsson, 2019). The corresponding MISR RA analysis suggests plumes dominated by medium, angular components (MeNspWab; Figure 2a). Each MISR RA retrieval for Phase A contains more than 20% small, spherical components (Figure 2b; supporting information) which, in volcanic plumes, would typically be interpreted as sulfates. However, the corresponding OMI record (Figure 2c) indicates minimal SO_2 emission (Figure 2c), a precursor to the formation of the small, spherical sulfate aerosols identifiable by MISR. It was widely reported from ground-based observations that Eyjafjallajökull erupted initially (14–16 April) through its summit glacier. This led to significant magma-water interactions, and the aerosolization of nonvolcanic water (e.g., Sigmarsson et al., 2011), likely altering the properties of the emitted aerosols. MISR plume Eyja2010b (see plume designations in the annotation of Figure 2) was observed by MISR furthest from the source (~1,800 km southeast: see Eyja2010b in the supporting information). Eyja2010b contained larger particles (MeNspWab plus MsSpNab) compared to Eyja2010a and Eyja2010c (MeNspWab plus SmSpHab(s), SmSpMab(f), and SmSpMab(s)). Increased particle size and angularity could represent downwind conversion and/or aggregation of aerosols during transport, or changes in erupted material over time. To fully explore the downwind alteration of this plume we would need observations of the same feature at multiple times during transport, which are not available in this case but are discussed subsequently in relation to observations at Grímsvötn. The presence of the glacier at the summit during Phase A impeded observations of any nascent lava flows. Correspondingly, no MODIS thermal anomalies were detected during this phase (Figure 2c).

MISR retrievals of plumes emitted during Phase B are characterized by an increase in REPS, driven by retrievals dominated by large components, some as nonspherical (LaSpNab, MeNspWab, and LaSpdWab: Figure 2), similar to those observed in Kamchatka (Flower & Kahn, 2018, 2020). The inclusion of the largest components, specifically LaSpNab and LaSpdWab, suggests the particles are at the upper limit of MISR retrieval size-sensitivity. The spherical *Whole Plume Particle Proxy* (Figure 2a) does not necessarily imply that spherical particles were present; rather, it is likely due to a lack of larger angular particle optical models within the RA algorithm climatology. The increase in REPS, combined with a corresponding decrease in REPA (Figure 2) between Phase A and Phase B, suggest a change in eruptive behavior, for example, alteration of the magma fragmentation mechanisms or magma composition. An initial burst of MODIS thermal anomalies during Phase B was followed by a decrease during the final week of April. Thermal activity resumed around 1 May, suggesting the start of a new eruption phase. However, corresponding changes in MISR RA and OMI analyses highlight that a change in emitted plume particles did not occur until around 5 May (Figure 2c), so we infer that the increase in thermal anomalies represents an eruption precursor. We note that Eyja2010e, at the beginning of Phase B, displays characteristics distinct from other Phase B plumes. The large angular particles and plume elevation below 2 km are common features of remobilized ash plumes (Flower & Kahn, 2017b). Eruption reports from the Icelandic Met Office (IMO) indicate that no corresponding plume was observed on radar, implying any emissions were confined below 3 km (Icelandic Meteorological Office, 2010), which is common for remobilized plumes (Flower & Kahn, 2017b). The lack of small, spherical components and SO_2 detections during Phase B suggests that this phase might represent the clearing of a pulse of volatile-poor magma stored at shallow depths prior to the onset of renewed activity.

Phase C entailed a resurgence of plume observations by MISR beginning on 5 May 2010, and correlated with a distinct increase in SO_2 emissions and thermal anomaly detections (Figure 2c). The MISR RA retrievals that coincide with high OMI SO_2 observations (Eyja2010j, Eyja2010k, Eyja2010l, and Eyja2010p) display decreased REPS and increased REPA. The overall REPS remained consistent through Phase C. However, the REPA and particle angularity vary markedly. Greater fractions of small, spherical components (VsSpNab, MsSpNab, SmSpHab(f), SmSpHab(s), SmSpMab(f), and SmSpHab(s)) were retrieved compared to previous plumes (Figure 2 and Table S3). However, these plumes still remain dominated by medium-

large, nonspherical retrievals (MeNspWab, LaSpdWab, and LaSpNab), suggesting ash-rich emissions with a small sulfate component. The majority of these small components were also categorized as light-absorbing (SmSpHab(f), SmSpHab(s), SmSpMab(f), and SmSpHab(s)), which is not typically characteristic of pure sulfate. Similar observations were made at Kliuchevskoi volcano in Kamchatka, Russia, where combined sulfate-ash plumes produced MISR RA retrievals containing up to 70% small, spherical, absorbing components (Flower & Kahn, 2020). The combination of small sulfates and larger absorbing ash particles within a plume causes the MISR RA to select the best fit for the aggregate of particles imaged within each 1.1 km pixel. As discussed in section 2.1.2, this leads to the selection of a mixture that can account optically for the small size of the sulfates, but also for the absorbing nature of ash. Within Phase C, we also identify two plumes having medium-large particles dispersing at low altitudes (Eyja2010m – 11 May; Eyja2010o – 13 May). Ground-based eruption reports detail plumes reaching ~6 km on these days but do not identify any observations of low altitude features. The discrepancy between the ground-based observed plume height and the satellite observations likely results from the limited sampling of the satellite instrument (an observation every ~1–2 days with MISR). However, on 12 May "Ash Mists" were reported by local observers (Icelandic Meteorological Office, 2010), corroborating our retrievals during this period. Ash Mist events are the result of the remobilization of previously deposited particles, lofted and transported near-surface. Such events represent significant hazards to local populations (Liu et al., 2014). The last plume imaged by MISR during Phase C (Eyja2010q; 16 May), corresponds to the final thermal anomaly cluster and the beginning of SO_2 emission decline. The concurrent decrease in observations made with MISR, OMI, and MODIS indicate the waning of this eruption.

Phase D covers the period of declining activity, with minimal plume emissions and sulfate observations. We reviewed the imagery beyond the active plume generation period to identify any secondary eruption factors. At Eyjafjallajökull, a single low-altitude, large component (MeNspWab, LaSpNab, and LaSpdWab) plume, characteristic of a remobilized ash plume, was observed during this period (Eyja2010s). No ash eruptions were identified on this day, but local reports do indicate that visibility was poor due to ash being "blown up" around the volcano (Icelandic Meteorological Office, 2010). This represents a significant particle remobilization event, highlighting the ongoing hazard posed by volcanic eruptions beyond the termination of active plume or flow emission. The longevity of these hazards is dependent on the geographical and climatic conditions of the region and the quantity of emplaced deposits. An extreme example of volcanic-deposit remobilization is Katmai (Alaska), where deposits initially emitted in the 1912 eruption were remobilized as recently as 2016 (Flower & Kahn, 2017b). In Iceland, minimal vegetation and relatively flat terrain make deposits particularly susceptible to lofting, as near-surface winds can scour the terrain unimpeded. A study by Liu et al. (2014) provides a detailed review of a significant Eyjafjallajökull remobilization event that occurred in 2013, three years after the termination of the 2010 eruption. However, after a significant gap between the eruption and a remobilization event, the resulting particles could be comprised of a combination of volcanic, fluvial and/or glacial deposits (Butwin et al., 2019; Liu et al., 2014).

4.1.2. Satellite Inferred Plume Processes During Transport

At Eyjafjallajökull, three plumes, for which we have MISR RA retrievals, appear to be transported through meteorological cloud (Eyja2010a, Eyja2010c, and Eyja2010k). In these plumes (e.g., Figure 3a), medium, nonspherical components (MeNspWab) are identified throughout, but small spherical components (SmSpHab(s), SmSpMab(f), and SmSpHab(s)) are predominantly found within ~ 150 km of the source, changing to medium spherical components (MeSpNab) up to 250 km downwind (Figure 3a: see supporting information for full plume particle-type maps.) The mixed aerosol-type retrieval (SmSpMab, MsSpNab, and MeNspWab) evolves toward a singular medium angular component (MeNspWab), increasing the overall REPS for the downwind plume segment. This suggests a change from a mixed sulfate/ash plume to an ash-rich plume. The depletion of small, spherical components likely represents the hydration, and possible activation, of the sulfate components. ("Activation" describes the transition of cloud condensation nuclei [CCN] to cloud droplets.) This would lead to the growth of particles beyond the ability of MISR to retrieve particle microphysical properties, and subsequent incorporation of these aerosols as cloud droplets (Figure 3c). In these instances, cloud processing and/or wet deposition of sulfates are possible. As the hydrophilic sulfate components grow to particle sizes beyond the retrieval sensitivity of MISR Vis-NIR observations (approximately 0.06–2.4 μm; Table 2), the relatively hydrophobic ash particles could remain unaffected (Figure 3c). We posit that, due to the greater likelihood for activation of sulfates vs. ash, mixed

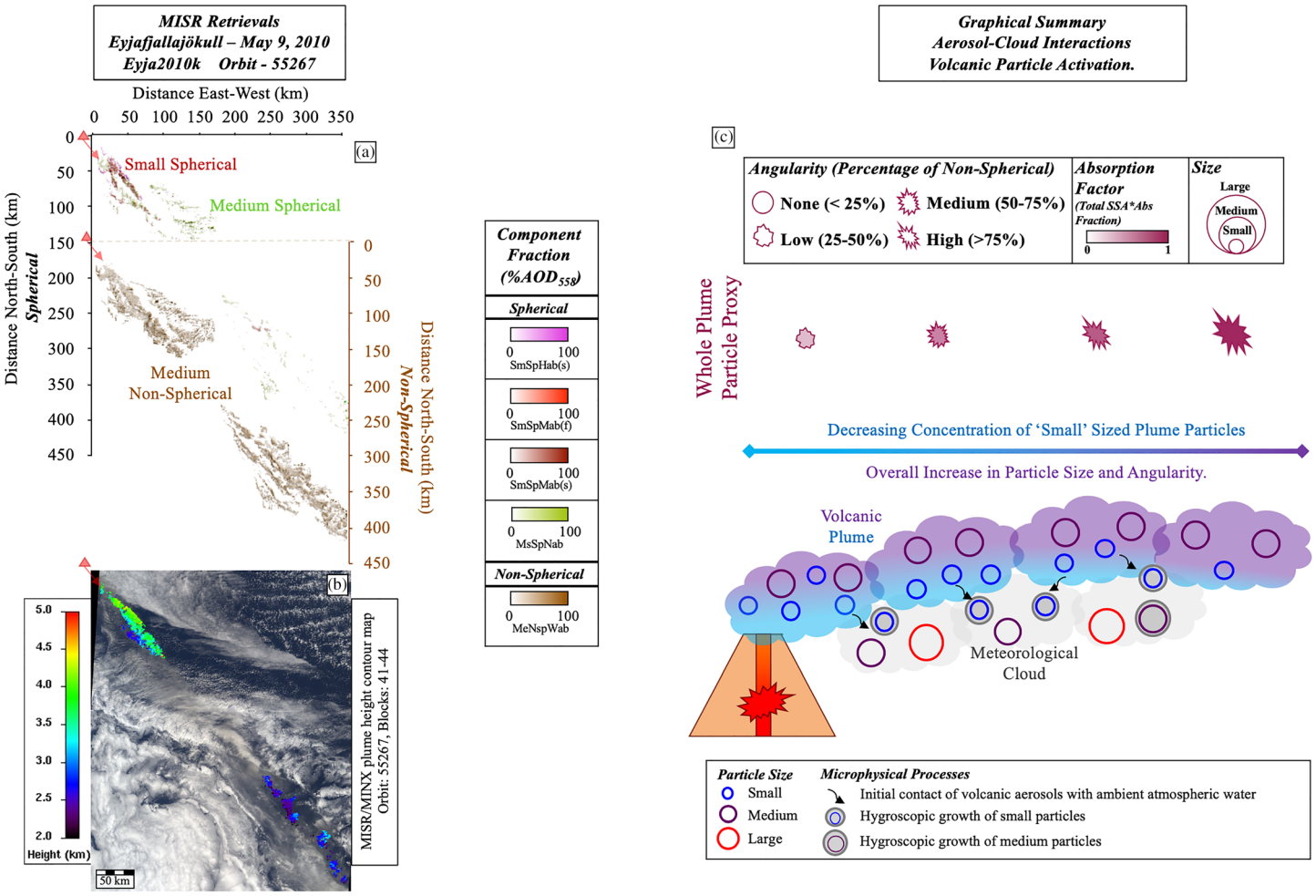

Figure 3. Eyjafjallajökull eruption plume imaged on 9 May 2010, incorporating (a) MISR RA plume particles, presented in map view (left axis: spherical components; right axis: nonspherical components) (detailed particle-type component information is given in Table S1 – MISR_RA_TABLE); (b) MISR plume-height contour map of volcanic emissions; (c) schematic model of plume particle transport and evolution derived from observed signals; and (d) cartoon illustrating relative particle size, shape, and absorption variations across the plume, inferred from MISR particle retrievals.

plumes emitted into a water-rich atmospheric layer can become depleted of the smaller sulfate components (VsSpNab, SmSpNab, and MsSpNab), leaving retrieved downwind plume features dominated by ash particle proxies (MeNspWab and LaNspWab; e.g., Figure 3a). Alternatively, some sulfate could evaporate or be lost as distinct MISR optical components by becoming coatings on the ash particles, though the persistent nonspherical shape in the retrievals makes the latter option appear less likely.

At Eyjafjallajökull, four plumes display decreasing REPS downwind, driven by increases in small, spherical components (Eyja2010j, Eyja2010l, Eyja2010n, and Eyja2010q). These retrievals include light-absorbing spherical components, which suggests the plumes contained some ash. Decreasing REPS with distance can indicates either deposition of larger particles and/or the formation of new, small aerosols from gaseous emissions. In these plumes, the AOD increases, suggesting that new particles formation is likely occurring, along with minimal particle deposition, leading to an increase in the retrieval of small, spherical components (e.g., VsSpNab and SmSpNab) and decreasing the REPS downwind. High OMI SO_2 observations (Figure 1c) support the conclusion that the decreasing REPS represents the conversion of SO_2 to sulfates as the plume ages. Existing literature establishes an order-of-magnitude increase in aerosol components 100 km downwind when comparing ground-based $SO_2/PM_{2.5}$ ratios (Ilyinskaya et al., 2017) and attributes this observation to the formation of sulfates. ($PM_{2.5}$ refers to the mass of all particle types having diameter less than 2.5 μm, usually assessed at the surface.) In the MISR RA cases where sulfate aerosol formation is inferred, the observed changes occur in the initial 150 km of downwind transport. In these cases, aerosol

formation is apparently tempered by plume composition (e.g., exhaustion of gaseous sulfur) beyond 150 km; alternatively, local ambient conditions, such as interaction between the plume and meteorological cloud, could result in altered particle properties downwind from the source.

4.1.3. Satellite-Retrieved Particle Light-Absorption Compared to Suborbital Particle Composition

In the MISR RA analysis for Eyjafjallajökull volcanic plumes, we attribute the strength of light-absorption and its spectral profile to the optical properties of ash particles. Different particle absorption profiles might indicate different particle properties, varying chemical composition of the source magma, especially as observed near-source, or alternatively, particle evolution in the ambient environment. At Eyjafjallajökull, the absorption characteristics are distinct between the "eruptive" Phases A and C, and the "declining" Phases B and D. Phase D is excluded from the remainder of this section. The plume was comprised of remobilized particles, which tend be size selected, resulting in the dominance of the largest modeled component (LaSpdWab) which by default is weakly absorbing. Phase A is dominated by spectrally steep absorption (stronger absorption in the blue spectral band) of moderate strength (SmSpMab(s) – SSA 0.9). Near-source, erupted plumes in Phase C also display spectrally steep profiles, but the particles are more absorbing than those from Phase A (SmSpHab(s): Figure 2 and supporting information). Phases B and D particles have relatively weak, spectrally flat absorption (SmSpMab(f) plus MeNspWab). To consider if these remotely derived patterns are related to underlying magma composition, we compare the pattern of variation in our results with ground-based sampling of tephra silica content (Gudmundsson et al., 2012; Laeger et al., 2017). A comprehensive overview of ground-based particle composition throughout the 2010 eruption was obtained from the work of Gudmundsson et al. (2012). Broadly, trachyandesite particles were emitted throughout the eruption (Phases A, B, and C). "Eruptive" phases (A & C) additionally generated particles of trachyte composition, with Phase A also producing rhyolitic deposits, unique to that eruption phase. We posit that the increased weight percent (wt. %) of silica (SiO_2) in trachyte and rhyolite particles compared to trachyandesites may have led to the variation in plume light-absorption across the eruption. Size-sorting during deposition and/or remobilization could also contribute to, or even account for, the retrieved spectral properties in this case; field validation data would be needed to resolve the ambiguity. Overall, the ash-rich plumes of Eyjafjallajökull show much steeper spectral absorption compared to the generally flat absorption profiles of plumes observed in Kamchatka (Flower & Kahn, 2018). The Kamchatka eruptions contained basaltic-andesitic rock, characterized by lower alkali content (wt. % $Na_2O + K_2O$) than those in Iceland. Although higher alkali concentration might account for the steeper spectral profiles for Eyjafjallajökull, a larger sampling of MISR RA analyses would be required to develop confidence in any links between magma chemical composition and plume optical properties.

4.1.4. Comparison of Satellite-Retrieved Particle Size With Suborbital Observations

We use available, suborbital observations of Eyjafjallajökull plume emissions to help validate our interpretations of the space-borne measurements. At Eyjafjallajökull, two teams performed airborne observations of plumes transported across Northern Europe (Johnson et al., 2012; Schumann et al., 2011; Turnbull et al., 2012). These flights tracked changes in particle properties from the plumes they were able to sample. One flight over the north Atlantic on 2 May 2010 tracked particles with an effective radius (r_e) of 0.9 μm. Later observations, in the North Sea (13 May) and Northern England (16 May), indicate significantly smaller r_e of ~0.15 μm (Schumann et al., 2011). This decrease in particle size is mirrored in the MISR RA observations between Phase B and Phase C. Midsized particles (r_e: 0.13–0.5 μm) were observed, having up to an order of magnitude higher particle number concentration than the smaller (r_e: 0.005–0.08 μm) or larger ($r_e > 0.75$ μm) classes (Schumann et al., 2011). MISR RA retrievals at Eyjafjallajökull are dominated by the MeNspWab component (Figure 3b), which has an effective radius of 0.75 μm, with most plume retrievals also containing a measurable fraction of small spherical components ($r_e \sim 0.12$ μm). The aggregate of components decreases the combined REPS, correlating more closely to the midsized class bin used by Schumann et al. (2011). An additional factor in volcanic particle assessment is the angular nature of components. SEM investigations of Eyjafjallajökull ash samples, obtained from suspension, indicate highly nonspherical particles in the ~0.25–3 μm radius range (Johnson et al., 2012). Not optimized for volcanic eruptions, the MISR RA is limited in nonspherical components (MeNspWab and LaSpdWab). The medium size of the ash identified at Eyjafjallajökull (Johnson et al., 2012; Schumann et al., 2011) correlates well with the combined MISR RA derived REPS and nonsphericity. Comparisons between the MISR RA and suborbital in situ observations support the efficacy of the MISR RA for mapping qualitative

differences in dominant particle type in the Icelandic plumes. Where plumes are comprised of particles finer or coarser than the components currently used in the RA algorithm, the climatology would be less effective.

Published ground-based sampling does not specifically detail variations in the *microphysical* properties of the particles with effective radius <2 μm retrieved by the MISR RA. However, they can provide further indication of changing eruption dynamics, particularly where airborne sampling is limited or nonexistent. Where surface bulk samples vary significantly, concurrent variations in microphysical component properties are likely. Therefore, we compare published bulk samples to the MISR observations in Iceland to the extent possible, to establish whether covariation is observed. This amounts to comparing particle size distribution trends within the size range to which MISR is sensitive (<~2 μm), with the larger-sized particles that usually dominate in situ samples. Cioni et al. (2014) sampled deposits from five events during the 2010 eruption: Three samples correspond to Phase A within the current study, one to Phase B, and one to Phase C. The ground samples suggest a change in dominant particle size from ~4 mm (Phase A) to ~0.5 mm (Phase B), with a subsequent increase to ~1 mm in Phase C. This pattern appears inverse to that observed by MISR, where particle size increased in Phase B then decreases into Phase C. However, the particles collected at the surface are orders-of-magnitude larger than anything that could be constrained with MISR observations (section 2.1.2). Yet, the bulk sampling also indicates a spike at ~1 μm (in the MISR RA "large" particle range) during Phase B. The increase in bulk sampled particles within the submicron-to-micron range, to around ~1–2 μm, would produce an increase in the MISR RA derived REPS, as observed. The concurrent particle variations between these measurement techniques highlight how noncomparable bulk sampling and remote sensing data might be used in combination to infer more detail of changing eruption dynamics than could be ascertained from a single technique.

4.2. Holuhraun, September 2014 to March 2015

Unlike the other Icelandic volcanic eruptions observed by MISR, Holuhraun consistently produced sulfate-dominated plumes during its late 2014 to early 2015 eruption. Eleven plumes were analyzed with the MISR RA in the initial two months of the eruption (Figure 4). Detailed passive observations from MISR, OMI, and the MODIS visible channels were impeded by low sunlight levels beginning in November, as winter approached (Figure 2c; low-light threshold, LLT). However, radiating hotspots, generated by lava flows and observed in the MODIS thermal infrared channels, are reported for the eruption duration. The MISR RA retrievals are dominated by small, spherical, nonabsorbing components (VsSpNab and SmSpNab; Figure 4b), indicating plumes containing little or no ash in all cases, distinct from Eyjafjallajökull (Figure 2). Retrieved particles are uniformly spherical throughout the eruption period, and significantly smaller than those typical of ash plumes (Figure 4a and Table S3). Figure 4d illustrates our interpretation of the aggregated remote-sensing observations in terms of the underlying factors driving the 2014–2015 Holuhraun eruption that are discussed in detail throughout this section.

4.2.1. Satellite Inferred Eruption Chronology

In contrast to Eyjafjallajökull, volcanic plume aerosol components at Holuhraun remained relatively constant over time; variations were small, and apparently driven by local meteorological conditions rather than magmatic variations, as discussed previously. However, the MISR-derived plume-height record at Holuhraun (Figure 4c) indicates generally decreasing ejection altitude between September and November 2014. Plume height is commonly used as an indicator of explosivity and is a key factor in assessing eruption magnitude through the Volcanic Explosivity Index (VEI) classification system (Newhall & Self, 1982). Therefore, we interpret the observed plume-height decrease as a mild reduction in ejection energy. Two possible explanations for this trend are: a shift to less vigorous effusion, also represented by lava flow extension at the surface, or eruption waning. OMI and MODIS aid in distinguishing between these scenarios. The OMI data indicate a slight decrease in SO_2 emissions by mid-September, but significant SO_2 emissions (>20 kt/day) persist until the OMI signal is lost beyond the November low-light threshold (LLT). The MODIS thermal anomaly data, not limited by light levels, suggest persistent lava outflow after the LLT. Although the emissions continue, the long-term trend of the data indicates a reduction in radiance over time, diminishing until anomaly signatures cease in mid-late February (Figure 4c). From interpretation of the satellite signals, we conclude that the eruption maintains effusive flows but that the source was depleted as the outflow continued.

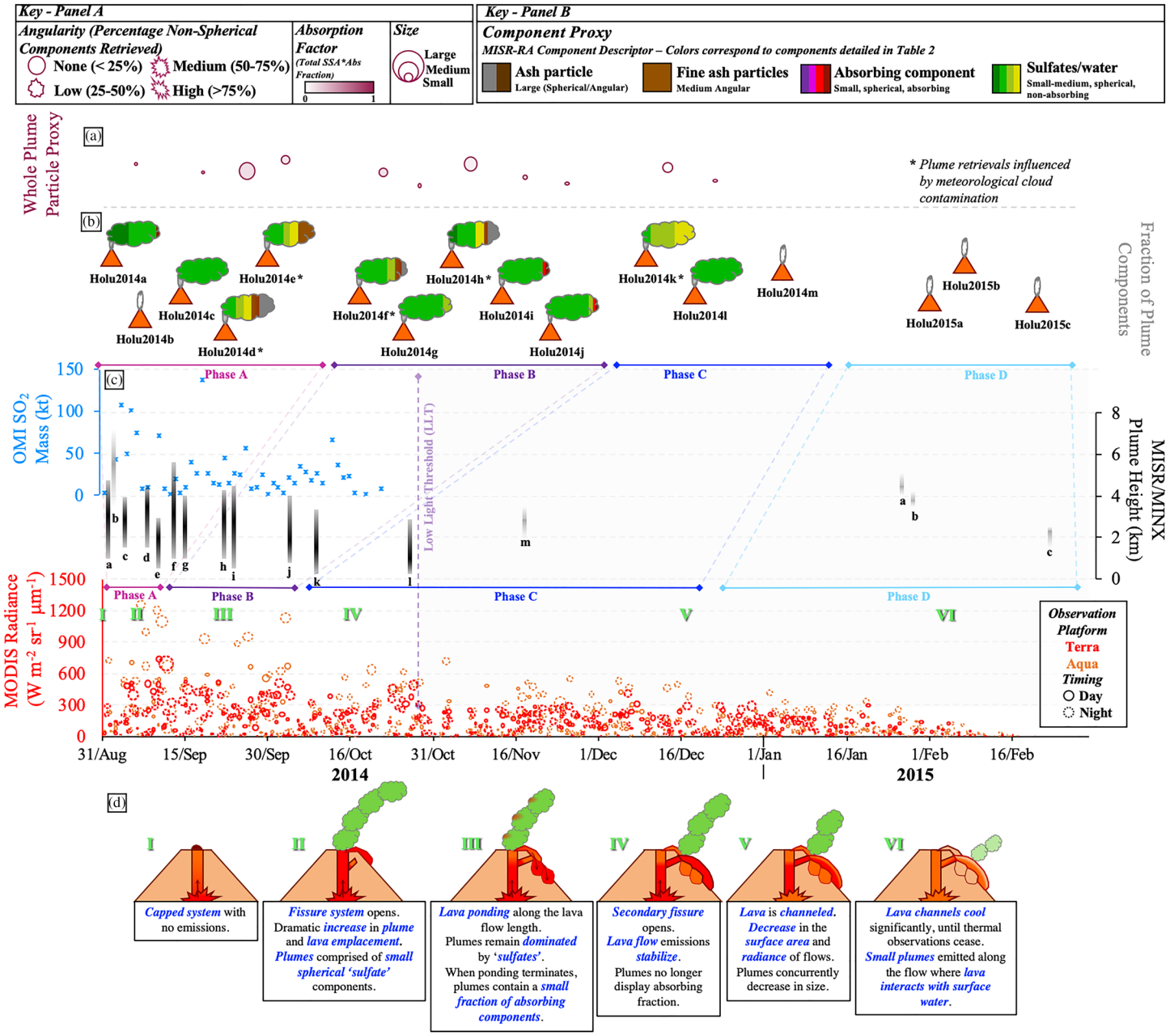

Figure 4. Timeline of remote sensing observations of Holuhraun eruption 2014, figure structure is the same as Figure 2. Note that MISR plume-height and OMI SO_2 data correlate to the MODIS timeline *x*-axis (at the bottom of panel c), whereas the plume and particle-type cartoons (panels a and b) are spread out for easier visibility. Colored lines at the bottom of panel (b) delineate and distinguish eruption phases and associate the cartoons with the timeline. Component color codes are given in Table 2. The MODIS data point size corresponds to the daily thermal anomaly count (range: 1–210 pixels in this case) as an indication of active radiating area. Full, individual MISR plume retrievals (MISR height, RA, and OMI data) and MODIS thermal anomaly data used to compile this figure are provided in the supporting information. Detailed analysis from which geological interpretations were derived is included in section 4.2.

The MODIS thermal anomaly record is our primary remote-sensing indicator of changing volcanic phases at Holuhraun. This time-series (Figure 4c) can be classified broadly into four periods: eruption ramp up (Phase A: 1–14 September); stable to gradually decreasing emissions, Phase B, (15 September to 4 October) and Phase C (5 October to 18 December); and rapidly decreasing emissions (Phase D: 19 December to 28 February). Ground-based observations of lava-field extent and evolution identified three phases of lava emission at Holuhraun (Pedersen et al., 2017): channel-fed lava transport (31 August to mid-October) corresponding to the period of Phases A and B (Figure 4d, II); lava ponding (mid-October to mid-December)

encompassing Phase C (Figure 4d, III); and tube-fed lava transport (late-December to 27 February) correlating to Phase D (Figure 4d, V–VI). Although the differences in eruption phases are not as distinct as those identified at Eyjafjallajökull, the remote sensing and ground-based observations are in general agreement. Transitions identified in the remote sensing data tend to lag behind the corresponding ground manifestations; this is most likely due to sampling limitations in the satellite record. Also, the earliest phase derived from our remote-sensing data (Figure 4c; Phase A) is not detailed in the suborbital record.

The eruption "ramp up" (Phase A) consists of 5 days of moderate surface thermal emissions (<300 W m^{-2} sr^{-1} μm^{-1}), followed by a rapid increase to >1,200 W m^{-2} sr^{-1} μm^{-1} in the MODIS data. The highest number of observed thermal-anomaly pixels in a single overpass (210), representing the largest hot-spot area, occurred on 12 September (Figure 4c; Phase A). The peak in radiant power and the coincident peak in SO_2 emissions mark a shift in volcanic activity after this point (Figure 2c, Point II).

Thermal anomaly detection during Phase B (15 September to 4 October) was stable to gradually decreasing, with emissions consistently reaching ~500 W m^{-2} sr^{-1} μm^{-1}. Plume particle properties retrieved for the two MISR-imaged plumes at the end of Phase B (Holu2014i and Holu2014j) were unique for the 2014–2015 eruption, containing 12% and 10% moderately absorbing components, respectively. These absorbing components were only retrieved within ~100 km of the source, suggesting rapid fallout or chemical alteration of aerosols. The distinct MISR-retrieved particle properties toward the end of Phase B may represent the depletion of a magma pulse prior to the onset of a secondary flow generating a minor fraction of fine ash that is deposited rapidly near the volcanic source. Ground observations highlight a switch in primary flow emplacement in October (Icelandic Meteorological Office, 2015), which corresponds to the development and subsequent cessation of plumes containing minimal absorbing components at the end of Phase B (Figure 4; Holu2014i and Holu2014j). The lack of evidence of ash emissions from Holuhraun, combined with the location of the volcano in the dust-rich highlands (Stefánsson et al., 2017), leads us to infer that the minor absorbing component observed in Phase B likely originate from the lofting of dust particles subsequently transported within the plume. However, the fact that these were not retrieved as the "dust" model in the RA (MeNspWab) suggests that any ash was present in very low concentrations and strongly dominated by sulfates in the retrieval. At this point in the eruption (early October), the frequency of plume observations also decreased (Figure 4c). As the lava is channeled into a tube-fed regime (Pedersen et al., 2017), decompressive events become less significant, which moderates plume generation and favors more effusive eruptive activity.

A distinct change occurred on 5 October, as thermal emission decreased to ~300 W m^{-2} sr^{-1} μm^{-1} (Figure 4c; Phase C). Initial plumes identified in Phase C were ejected below about 2 km altitude (most earlier plumes were ejected to around 4–5 km), suggesting a reduction in explosivity concurrent with a decrease in SO_2 emissions (Figure 4c). Ground-based observations around this time report plumes at an altitude of ~1–3 km (Icelandic Meteorological Office, 2015). The majority of Phase C occurred following the LLT, so OMI and most MISR products are unavailable. However, the MODIS thermal anomalies show persistent, though declining, lava emissions. They cover progressively smaller areas (marker size; Figure 4c) and display lower radiant power (Figure 4c), likely corresponding to the formation of lava tubes that reduce the direct observation of exposed lava features from space. After November 2014, low light level, small plume size, and high surface albedo due to snow cover preclude MISR particle property analyses. However, four plumes were identified in the MISR imagery after LLT on which plume-height retrievals were performed (Figure 4c). Post-LLT emitted plumes were confined to smaller areas (60–685 km^2) than earlier plumes (5,490–43,630 km^2). Holu2014m was more energetic (Figure 5a) than plumes emitted in 2015 (Figures 5b–5d). OMI was unable to retrieve SO_2 concentrations during this period. However, SO_2 emissions were observed by the European Space Agency's (ESA) Infrared Atmospheric Sounding Interferometer (IASI) showing an increase in SO_2 emissions prior to the observation of the Holu2014m plume (Carboni et al., 2019). Holu2014m is therefore likely a more vigorous event driven by a volatile-rich magma pulse, distinct from later passive degassing from the cooling flow surface.

The exact point of Phase C-D transition in the plume record is somewhat ambiguous due to the reduced plume data coverage caused by the LLT. We define the Phase C-D transition point relative to a ~5 day decrease in thermal output (Point V in Figure 4c). During this period the thermal anomalies records indicate emplacement evolution. Prior to 20 December 2014 the flow has a linear core of highly radiating pixels. After

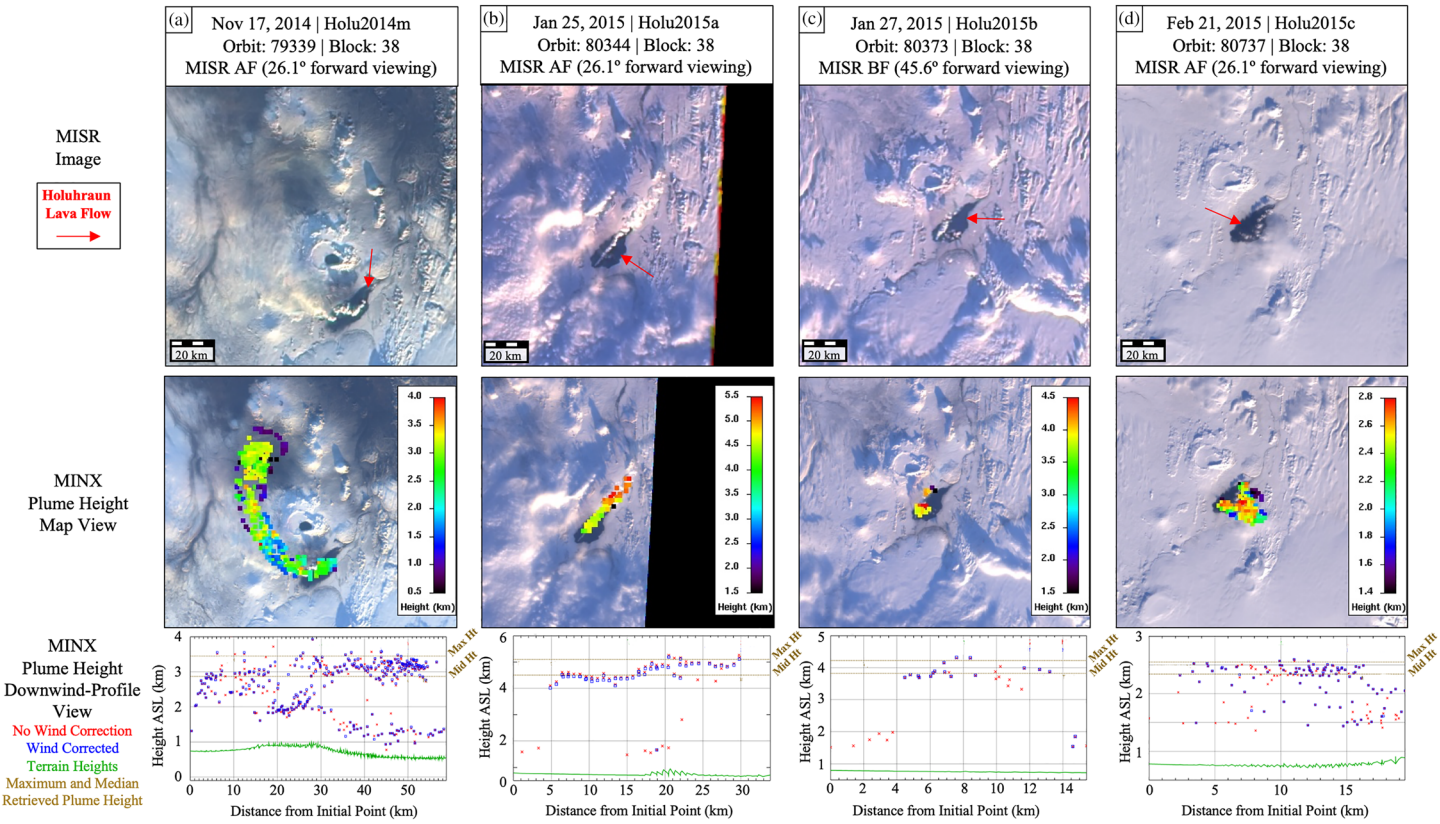

Figure 5. MISR plume observations at Holuhraun volcano, November 2014 to February 2015, including (top row) MISR images of eruption plumes, with observation date and event label, orbit and camera information detailed above. The location of the lava flow field, from which plumes are emitted, is highlighted in each image by a red arrow; (middle row) MISR plume height analysis in map-view; (bottom row) MISR plume height retrievals in downwind-profile view. Note that these MISR-imaged plumes occurred after the low light threshold (LLT) was crossed in late October 2014, as indicated in Figure 4.

20 December, the highly radiating pixels become confined to the primary vent area, with sporadic high radiance observed at the eastern edge of the flow field. The disconnect between the two highest radiating points could be explained by the formation of lava tube systems, insulating the flow between the initial point of emission (main vent) and the edge of the flow field (tube terminus). We interpret this as representing an initial tube-forming stage, when observation of the highly radiant lava is impeded by the lava tube crust (Figure 4d, V–VI). Ground-based observers also report the development of lava tubes, or closed channel systems, during this period (Icelandic Meteorological Office, 2015; Pedersen et al., 2017). By the end of January, the overall area of the flow decreased substantially (MODIS marker size; Figure 4c), with the primary radiant energy emitted by two distinct regions: over the vent and at the northeast extent of the flow field (likely at the lava tube terminus).

Two of the Phase D plumes (Holu2015a and Holu2015b) were ejected to higher altitudes than the majority of plumes in Phases B and C; however, they are comparable with the upper extent of plumes emitted in Phase A (Figure 4c). The increased emission altitude of these plumes is likely more a function of the temperature contrast between the hot volcanic emissions and the cold, wintertime ambient atmosphere than of increased explosivity. Plumes observed during this period were small (<200 km^2) relative to plumes observed in the early stages of the eruption (580–26,000 km^2), more indicative of mild degassing from the remaining cooling lava (Simmons et al., 2017). The final plume (Holu2015c) appears diffuse (Figure 5d) and is not clearly emitted from a single point, unlike those observed earlier in 2015 (Figures 5b and 5c). The cessation of thermal anomaly retrievals before this event, the low altitude of the plume and the undefined source at the edge of the flow, suggest that the plume is the result of residual heating of the snow surrounding the flow perimeter. Qualitative visual assessment of the 2015 plumes found no evidence of ash composition (e.g., dark

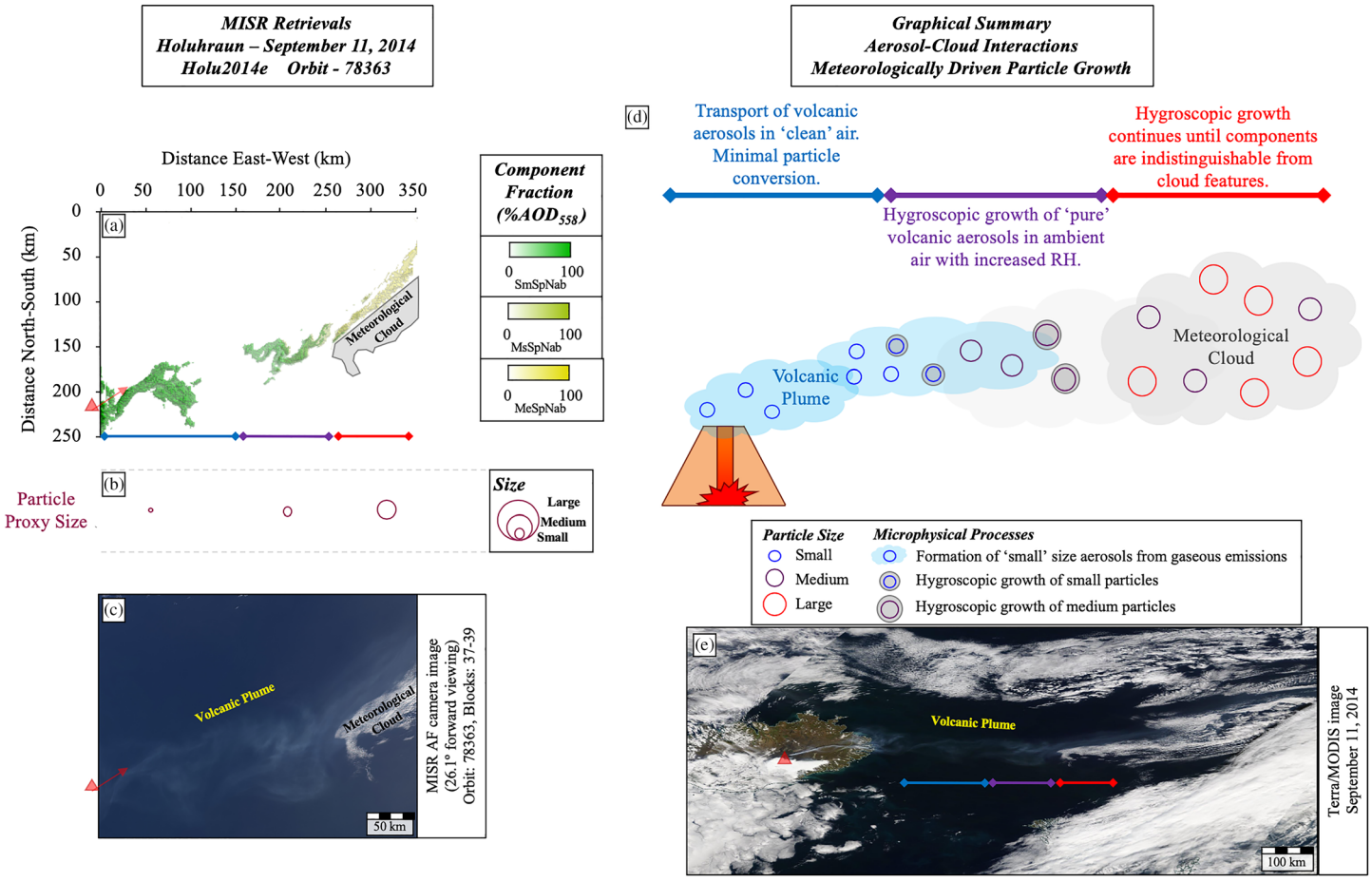

Figure 6. Holuhraun eruption plume imaged on 11 September 2014, incorporating (a) MISR RA plume particles, presented in map view (detailed particle-type component information is given in Table S1 – MISR_RA_TABLE); (b) relative particle size variations across the plume, inferred from MISR RA particle retrievals; (c) MISR 26.1° forward-viewing (AF) camera true-color image of the plume; (d) schematic model of plume particle transport and conversion, interpreted based on remote-sensing data. (e) MODIS broad-swath context image, showing the relationships between the volcano source (red triangle), meteorological cloud, and three downwind segments of the Holuhraun plume (colored arrows in panels e and a).

plumes, dark deposits on the snow-covered ground downwind; Figure 5), supporting the theory that these plumes represent degassing from the remaining open vent rather than discrete explosive events. The reduced emission of lava (decreased MODIS thermal anomaly detections; Figure 4c), combined with the decreasing size of the eruption plumes (Figure 5), indicate a waning eruption, terminating in mid-late February 2015. The change in eruptive style between Phase C and Phase D correlates approximately with a significant reduction in the SO_2 reported from IASI (Carboni et al., 2019).

4.2.2. Satellite-Retrieved Individual Plume Properties

About half the Holuhraun plumes in our dataset (Holu2014a, Holu2014c, Holu2014e, Holu2014h, Holu2014i, and Holu2014j) show increasing AOD in the initial ~150 km of the plume. These retrievals are dominated by small, spherical, nonabsorbing components (VsSpNab and SmSpNab) characteristic of sulfate aerosols. Therefore, we posit that processes in the near-source plumes tend to be dominated by the conversion of gaseous SO_2 (invisible to the MISR instrument) to sulfate aerosols (H_2SO_4), similar to those previously identified at Eyjafjallajökull (see section 4.1.2).

Five MISR-imaged plumes (Holu2014d, Holu2014e, Holu2014f, Holu2014h, and Holu2014k) also display evidence of additional downwind plume evolution, with particle size increasing as the plume retrieval nears an area of meteorological cloud. Holu2014e provides an ideal case for investigation of these processes (Figure 6). Initially transported through a relatively clear atmosphere (Figure 6e), the MISR RA retrievals report minimal change in component properties (SmSpNab). As the plume transited into the cloud

boundary region (150–350 km downwind), MISR RA retrievals show an increase in REPS (Figure 4b and Holu2014e_78363 in the supporting information). The apparent growth of aerosols in the plume most likely represents the hydration of volcanic sulfates. Growth of sulfates can eventually lead to the particles acting as CCN (Figure 6d). Direct observation of particle activation is outside the capabilities of the current technique, due to the ~2–3 μm upper bound on particle size retrieval sensitivity. Although cloud contamination in the retrieval process could be a contributing factor, particle hygroscopic growth and possible activation seem likely in this case, given the retrieved particle properties and meteorological context. Further, ground-based radar and balloon observations support the interpretation that aerosols originating from the volcano interacted with meteorological cloud, likely serving as CCN (Pfeffer, 2018; Vignelles et al., 2016).

The furthest extent of the MISR-imaged plume adjoins an area of cloud located at the same altitude as the plume (Figure 6c). When the broad-swath MODIS image is considered (Figure 6e), the cloud region extends into an otherwise cloud-free atmosphere along the path of the volcanic plume. The alignment of this cloud along the volcanic plume path is further suggestive that volcanic aerosols could be acting as catalysts for the formation of cloud droplets. The meteorological cloud region is dominated by large, spherical, nonabsorbing components in the MISR RA retrieval (LaSpNab: see supporting information for full plume retrieval), indicating a size difference between pure volcanic plume and volcanic particles affected by ambient meteorology. Suborbital balloon measurements, obtained in January 2015 from a Holuhraun plume, indicate similar evidence of cloud-aerosol size variations (Vignelles et al., 2016). In their study, where the balloon passed through two plume layers, particle sizes varied based on whether hydration of the plume particles had occurred. The small-sized plume features displayed bimodal peaks in particle radii at 0.1 and 1.2 μm, whereas the larger, "hydrated" plume components exhibited bimodal peaks with radii of 1.1 and 9.8 μm. Based on the components included in the MISR RA, the initial plume particles would be retrieved as small-medium, spherical components. The hydrated particles would probably exceed the upper size limit of MISR retrieval sensitivity. Complimentary modeling studies, conducted on cloud feature development during the Holuhraun eruptions September–October 2014, found that the number of droplets in meteorological clouds increased and droplet effective radius decreased where volcanic particles were present (Malavelle et al., 2017), indicative of aerosol-cloud interaction.

4.3. Grímsvötn, 22–24 May 2011

Grímsvötn volcano reactivated in 2011, erupting for 8 days after 6 years of quiescence (Petersen et al., 2012). During this eruption, no MODVOLC thermal anomalies were identified. However, three plume features were observed by MISR. The 22 May 2011 event produced a complex, multilayer plume ideal for MISR multiangle investigation (Grim2011a; Figure 7). The two remaining plumes were imaged on 24 May: one near-source but obscured by clouds, and one downwind (Grim2011b), imaged to the northeast of the British Isles and originating from the 22 May eruption. The remainder of this section discusses the 22 May eruption. Plume structure and composition, as deduced from the aggregate of remote-sensing observations, are represented schematically in Figure 8. MISR plume-height retrievals identify three distinct aerosol layers concentrated at <2, ~7, and 12–16 km ASL (Figures 7a and 7b). Ambient atmospheric static stability, obtained from NOAA/ESRL Reanalysis data (Kalnay et al., 1996: https://www.esrl.noaa.gov/psd/map/profile/, last accessed April 2019), indicates that each plume layer is capped by a layer of peak atmospheric stability (Figure 7c). As observed in previous work (e.g., Kahn et al., 2007; Val Martin et al., 2010), aerosols tend to accumulate in layers capped by higher relative stability, as it is difficult to mix upward through a stable layer. The exact vertical location of plume peaks is mediated by the inherent buoyancy of the hot volcanic effluent. Overshooting of stable regions or upward turbulent mixing, and subsequent descent can occur until an altitude at approximate equilibrium is reached. Once this altitude is reached, suspended particles become more susceptible to gravitational sorting and settling processes. At Grímsvötn, MISR-retrieved plume heights indicate overshooting up to 16 km, with neutral plume buoyancy occurring in the umbrella plume region at ~12 km.

MISR RA analyses produced distinct particle property retrievals in each plume segment (Figure 8a). Large, nonspherical, light-absorbing particles (LaSpdWab) were retrieved in the lowest altitude feature, confined below 2 km (Figure 8a). This feature was most likely generated by selective, gravity driven particle deposition from the eruption column, as previously posited by Prata et al. (2017). Our MISR plume-height retrievals support this result (Figures 7a and 7b). The "noisy" MISR/MINX derived plume base (Figure 7b),

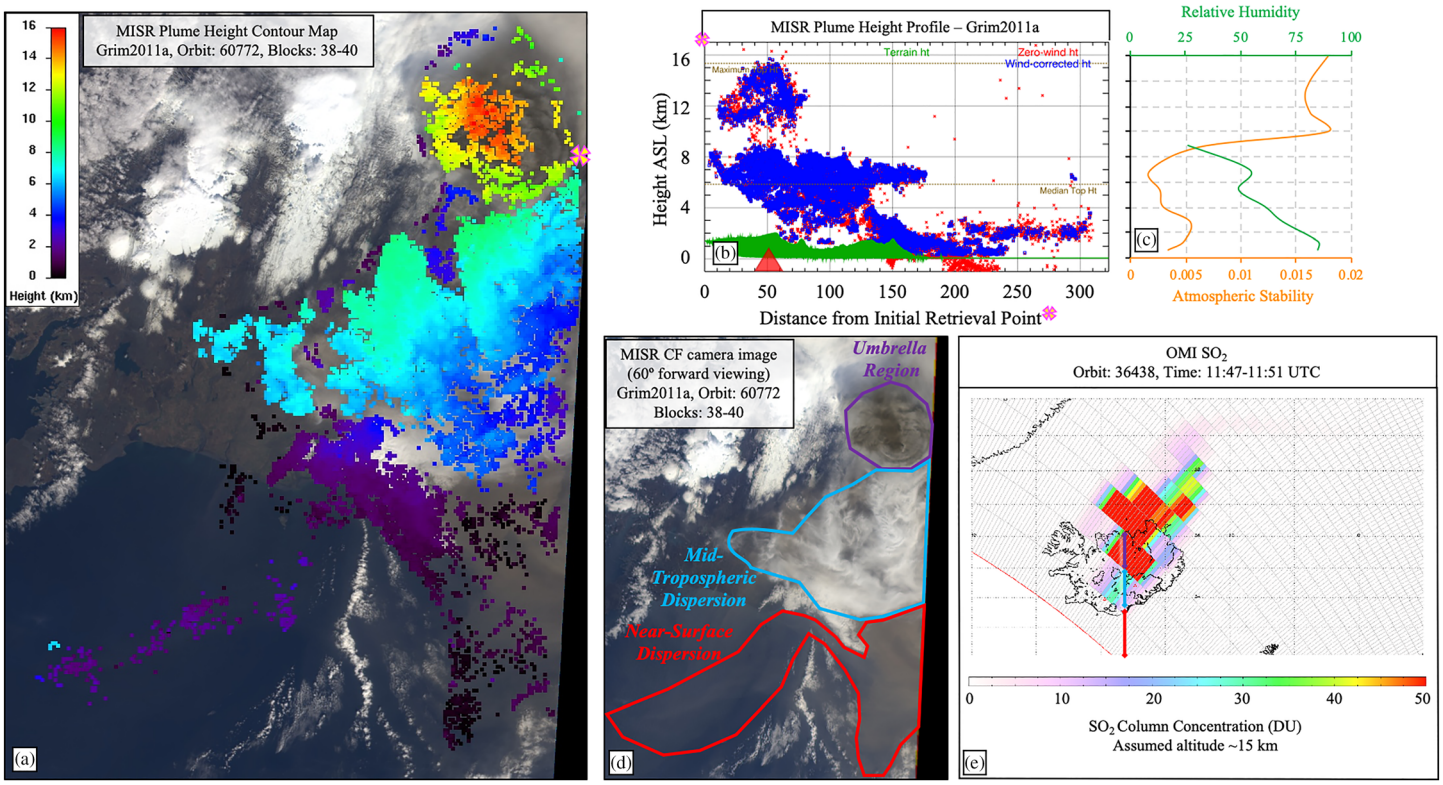

Figure 7. Plume observations of the 22 May 2011 eruption of Grímsvötn volcano, including (a) MISR plume height analysis in map-view, with the volcano location indicated by a red and white symbol along the right edge of the image; (b) MISR plume height downwind-profile-view; (c) local atmospheric static stability and relative humidity profiles corresponding to plume emission, from NOAA/ESRL reanalysis; (d) MISR 60° forward-viewing (CF) camera image of eruption plume, with plume layers delineated based on plume height retrievals; and (e) OMI SO_2 column concentration, assuming an injection altitude of 15 km.

with retrieved plume points distributed between the stable plume region at ~8 km and the ground, suggests significant particle deposition. Previous work has established that MISR can distinguish between particle-size-dependent gravitational settling and turbulent, size-independent deposition regimes in some cases (Flower & Kahn, 2020). As might be expected, the settling regime depends strongly on atmospheric stability structure, vertical wind shear, and plume buoyancy. Size-selective settling occurred for the Grímsvötn plume, as the MISR retrievals indicate considerably larger particle proxies in the near-surface layer than in the plume layers aloft (Figure 8b). Although the near-surface particles descended from the plume, at least some remained airborne. With sufficient wind shear or convection, Planetary Boundary Layer (PBL) mixing can dominate gravitational settling, impede deposition, and result in continued near-surface transport of these larger particles. The plume-height retrievals indicate uplift after this plume segment transits over the coastline, between 180 and 230 km downwind of the source (Figure 7b). This probably represents the transition of the plume from the turbulent planetary boundary layer to overriding the stable marine boundary layer, which further inhibits particle deposition. A similar pattern of dispersion has been observed in other cases for particles that are remobilized by turbulent mixing within the PBL after initial sedimentation (Flower & Kahn, 2017b).

The near-surface Grímsvötn plume was tracked by the ESA SEVIRI (Spinning Enhanced Visible and Infrared Imager) sensor in geostationary orbit for 3 days following emission (Cooke et al., 2014), and its location downwind on 24 May corresponds to the Grim2011b MISR-imaged plume. (The full plume retrieval is provided in the supporting information) The downwind observation of a plume, previously imaged by MISR, provides an opportunity to assess the influence of longer-range transport on particle characteristics. The SEVIRI image, corresponding to MISR plume Grim2011b, was the last observation of this plume by SEVIRI, and was characterized by a significant decrease in particle concentration relative to earlier observations by this instrument (Cooke et al., 2014). The MISR Grim2011b retrieval yields a midvisible AOD of over

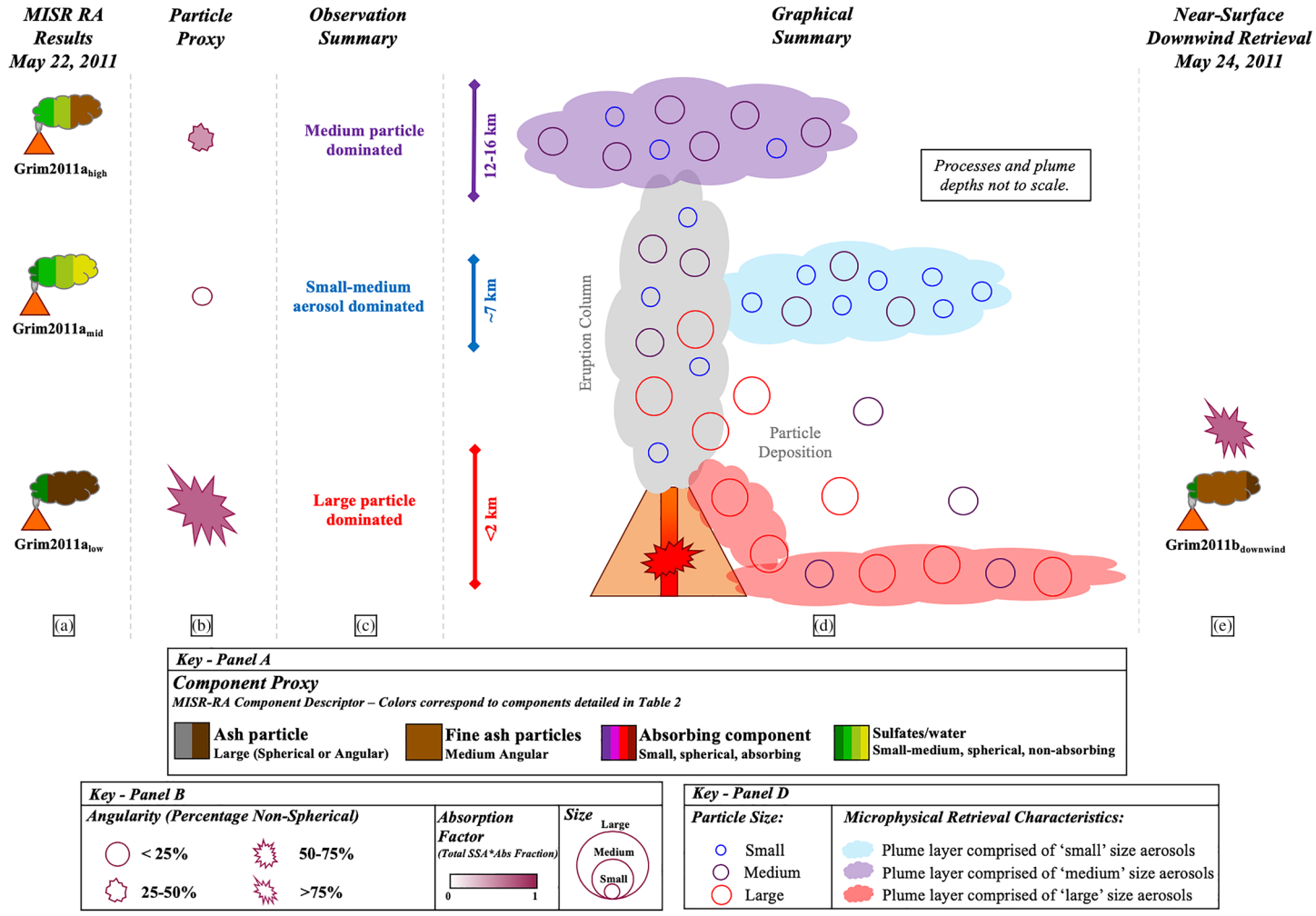

Figure 8. Interpretation of Grímsvötn eruption plume imaged on 22 May 2011, including (far left column) (a) MISR whole-plume particle component fractions, derived from MISR RA retrieval algorithm. (detailed particle-type component information is given in Table S1 – MISR_RA_TABLE); (middle left column) (b) whole-plume particle size derived from MISR RA retrieval algorithm; (middle column) (c) inferred plume layer particle type; (middle right column) (d) schematic model of plume particle structure and transport, derived from observed signals; and (far right column) MISR whole-plume particle component fractions and whole-plume particle size derived from MISR RA retrieval algorithm for the 24 May 2011 downwind plume feature. Note that plume layers discussed here are delineated on the visual imagery in Figure 7d.

2. However, the REPS is considerably smaller for the downwind retrieval (Grim2011b: Figure 8e), dominated by medium, nonspherical (MeNspWab) components, compared with large, weakly absorbing particles (LaSpdWab) that dominate near the source (Grim2011a_1km in the supporting information). The decrease in REPS (Figure 8e), is likely driven by size-selective gravitation particle deposition.

The middle plume layer was confined to a region of relatively low atmospheric stability spanning the 4–8 km altitude range (Figure 7c). This midtropospheric plume is visibly lighter in color than the plume layers above and below (Figure 7d). The MISR RA retrieves spherical, nonabsorbing components of varying sizes in this layer (Figure 8a), most likely sulfate/water-dominated particles. Further, these plume particles appear to grow in REPS as they age downwind from the eruption column (Grim2011a_7km in the supporting information). A region of meteorological cloud was located to the north of the plume, at a similar altitude to the identified volcanic feature. Based on NOAA/ESRL reanalysis meteorology, the cloud was being transported southeast, intersecting with the plume. A MISR RA retrieval in the vicinity of the northern cloud region is dominated by the large, spherical, nonabsorbing component (LaSpNab). Therefore, we posit that this ~7 km altitude feature represents a meteorological cloud affected by interaction with small volcanic aerosols in the eruption column. The volcanic particles could act as CCN, leading to the formation of an increased

number of smaller cloud droplets than would form otherwise. This also represents a pathway for particle activation, and possibly cloud processing of the aerosols. A review of both the Terra and Aqua MODIS visual data for the Grímsvötn eruption covering 22–24 May established that this feature was indistinguishable from the surrounding meteorological clouds after 24 hr, whereas the near-surface, ash-rich plume remained clearly visible (Figure S1).

The third plume layer considerably exceeded the local tropopause, which was present between about 9 and 11 km ASL (Figure 6c). This plume segment spreads uniformly from the volcanic column. Therefore, the starting point for MINX plume-height retrieval was placed at the MISR swath edge, rather than directly over the source, so the entire plume could be captured in a single retrieval. The location of the volcanic vent is marked by a red triangle in Figure 7b, and it lies directly below the peak elevation of this plume. When the MINX plume height is compared with the atmospheric static stability profile (Figure 7c), the peak in plume height surpasses the strong tropopause inversion, which peaks around 10 km, and reaches into the stratosphere. Plume top overshooting reaches as high as 16 km, though the greatest aerosol concentration falls between about 11 and 13 km, within the lower stratospheric stability layer (Figures 7b and 7c). The injection of the plume into the stratosphere indicates that this eruption is the most energetic observed so far by MISR in Iceland. Particle lifetime in the stratosphere is considerably longer than for particles in the troposphere (Sparks et al., 1997). Despite being impeded by the ORA (section 2.3), OMI retrievals track the significant injection of SO_2 into the stratosphere during this eruption, persisting until 31 May; volcano degassing at a lower rate continued through 9 June 2011. Local radar records established a plume height of ~15 km at the time of the MISR observation (Petersen et al., 2012), consistent with the MISR stereo-derived plume extent of 11–16 km (Figures 7a and 7b). The multidirectional spreading of the plume suggests either very low wind speed at altitude, or that this high-elevation plume was imaged shortly after ejection and did not have time to spread downwind by the time of observation. MINX wind vector retrievals indicate negligible along-track (roughly north–south) wind, but cross-track winds were perhaps 12 m/s, though with considerable scatter (Grim2011a_15km in the supporting information). The MISR RA retrieval suggests a plume comprised of medium aerosols (SmSpNab, MsSpNab, and MeNspWab), including a contribution from nonspherical components (Figure 7b). The OMI data highlight a significant concentration of SO_2 (Figure 7e) corresponding to the feature. Visible-band data from MODIS do not suggest persistent ash transport at high altitude on subsequent days. However, the OMI data show that the high-altitude plume layer was initially advected to the north before moving to the west over Greenland and Northern Canada for at least 4 days (Figure S1). The lack of visual signal, but continued OMI observations, suggests that ash was deposited from suspension, whereas the gaseous components were transported within the lower stratosphere, where conversion to sulfate particles is generally slower than in the troposphere. Previous work by Cooke et al. (2014) also identified decoupling of SO_2 and the main ash plumes in the 2011 eruption at Grímsvötn. Our observations substantiate this (Figure S1); the sulfate-rich plume advected to the north at high altitude (Grim2011a_15km) with no ash component beyond initial ejection, whereas the main, ash-rich plume moved south much nearer the surface (Grim2011a_1km).

The MISR RA retrieval result for the elevated plume region, in aggregate, was comprised of moderately-absorbing, somewhat angular, small-medium components (Figures 8a and 8b). When we consider the particle retrievals, the OMI SO_2 emissions (Figure 7e), and the visually dark nature of this plume, we deduce that the plume layer initially contained a mixture of SO_2 (Figure 7e), sulfates (SmSpNab and MsSpNab, Figure 8a) and fine ash particles (MeNspWab, Figure 8a). This combination of components is distinct from the ash-rich Eyjafjallajökull plumes, due to a significantly larger fraction of small-medium, spherical, non-absorbing components (SmSpNab and MsSpNab). Although apparently not impacted initially by gravitational deposition in the column, the fine ash particles, more susceptible to deposition than the sulfates, were apparently dropped from suspension or at least dissipated within the first 24 hr, leaving only the sulfate particles in the stratosphere for long-range transport.

The overall picture developed for the 22 May 2011 Grímsvötn eruption from the aggregate of remote-sensing observations is illustrated schematically in Figure 8d. As a well-mixed column of particles and gases is ejected from the volcano, particle sorting within the plume occurs, with the gravitational settling of larger particles. The column, now comprised primarily of gases and small-medium aerosol components, continued to rise, passing through an atmospheric layer containing meteorological clouds. Volcanic particles probably acted

as CCN, either altering existing cloud droplets or nucleating new ones. The concentration of small components is highest where volcanic particles were more abundant. This volcano-cloud interaction likely scavenges the small, spherical sulfate aerosols that are more hydrophilic than ash components. The eruption column continues to be lofted, until the plume buoyancy equalizes and upward motion ceases. The plume top, immediately following emission, is comprised of a combination of finer grained ash components (SmSpNab, MsSpNab, MeNspWab), and the SO_2 (Figure 7e) along with sulfate components not converted or deposited from the eruption column. Subsequent observations suggest the fine ash components from the most elevated layer either dissipated or were deposited from suspension following plume buoyancy neutralization.

5. Conclusions

Our review of volcanic activity in Iceland, as observed by NASA/EOS remote-sensing instruments, identified three eruptions, capturing 38 distinct plumes, of which 28 were appropriate for full MISR RA particle-property analysis. MISR, OMI, and MODIS data were incorporated into a multisensor analysis to produce comprehensive eruption timelines. Based on the remote-sensing data record, the three eruptions (Eyjafjallajökull 2010, Grímsvötn 2011, and Holuhraun 2014–2015) displayed distinct eruption dynamics and generated varied plume products.

At Eyjafjallajökull and Holuhraun, changes in plume properties observed from space resolved eruptive-style transitions during periods of persistent activity. Although the MISR RA analysis was not developed specifically for volcanic purposes, the results suggest that this technique can be used to study post-2000 eruptive events globally, particularly when combined with complimentary, daily UV, visible, and infrared observations from instruments such as OMI and MODIS. The limited particle size range distinguishable by MISR makes this technique most effective for separating sulfate- from fine-ash-dominated plumes, and for determining variations in these properties across eruptive events. The analysis of Eyjafjallajökull highlights the possibility of deducing qualitative variations in erupted magma composition, due to variations in plume-particle light-absorption strength and spectral dependence. The MISR retrievals warrant further validation, with diverse plumes types, to establish the technique's global applicability.

Additionally, we explored a complex, multilayer plume emitted from Grímsvötn in May 2011, using the unique plume-height observations available from MISR. The analysis of plume segments at different altitudes, and the corresponding segregation of retrieved particle properties, further demonstrate the capabilities of multiangle remote sensing. The specific altitudes of plume concentration, particle transport, and meteorological interactions presented here apply specifically to the 22 May 2011 eruption of Grímsvötn. However, the processes inferred to influence the segregation of particles during dispersion (e.g., particle deposition, accumulation of particles in layers of atmospheric stability, and plume-cloud interactions), are factors commonly affecting eruptive plumes elsewhere. As such, the combined analysis presented here could be applied to other complex, multilayered plumes for which MISR imagery is available.

In Iceland, the plumes displayed a range of compositions and dispersion characteristics. Due to the persistence of local meteorological cloud, plume-cloud interactions apparently influenced downwind particle development in some cases. Discernable processes varied depending on the initial composition of the emissions, the location and extent of moist layers and meteorological cloud, and the degree to which interactions occurred. Observed plume evolution in these cases can be classified into three general processes: downwind formation of aerosols; volcanic sulfate hydration and possible activation, and possibly particle cloud processing.

Work presented here details a variety of volcanological and meteorological processes of key importance in understanding lithosphere-atmosphere coupling. These deductions were made primarily through multisensor remote-sensing analysis. In order for such work to continue, Earth observing satellite systems must be supported, to capture new events and maintain data continuity.

Data Availability Statement

MISR data are freely available for download from NASA's MISR data repository (https://l0dup05.larc.nasa.gov/MISR/cgi-bin/MISR/main.cgi), maintained by NASA's Langley Research Center (LaRC)

Atmospheric Science Data Center (ASDC). The MISR INteractive eXplorer (MINX) program, for determining the altitude of plumes, is a stand-alone software package developed at the NASA Jet Propulsion Laboratory (JPL) and distributed through Github (https://github.com/nasa/MINX/releases). The MISR 774-mixture Research Algorithm (RA) developed and provided by Ralph Kahn and James Limbacher at NASA Goddard Space Flight Center. MISR RA and MINX results generated in this work can be accessed through the NASA Langley DAAC (https://asdc.larc.nasa.gov/project/MISR_Volcano_Research/ICEVOLC_FlowerKahn2020_1) (data https://doi.org/10.5067/Terra/MISR_Volcano_Research/ICEVOLC_FLOWERKAHN2020_1). Thermal anomalies, derived from MODIS data, are obtained through the MODVOLC hotspot alert system operated by the Hawaii Institute of Geophysics and Planetology, a division of the University of Hawaii, Manoa (http://modis.higp.hawaii.edu). MODIS true color imagery accessed through the NASA Worldview application (https://worldview.earthdata.nasa.gov), part of the NASA Earth Observing System Data and Information System (EOSDIS). OMI Level 2 total column SO2 (OMSO2) data are publicly available from NASA Goddard Earth Sciences Data and Information Services Center (NASA GES DISC, 2016; http://disc.sci.gsfc.nasa.gov/Aura/data-holdings/OMI/omso2_v003.shtml). The OMI processing code used to analyze this data (OMIplot), developed and provided by Simon Carn through the Vhub (2016) website (https://vhub.org/resources/682). OMPS imagery obtained from the Global Sulfur Dioxide Monitoring Home Page administered by NASA Goddard Space Flight Center, Atmospheric Chemistry and Dynamics Laboratory (https://so2.gsfc.nasa.gov/index.html). NCEP Reanalysis data for ambient meteorological assessment are provided by the NOAA/OAR/ESRL PSD, Boulder, Colorado, USA, from their website (https://psl.noaa.gov/).

Acknowledgments

The work of Verity J. B. Flower is supported by a NASA-ROSES Earth Surface and Interior (ESI) grant (NNH18ZDA001N-ESI) administered by Universities Space Research Association within the GESTAR program. The work of Ralph Kahn is supported in part by NASA's Climate and Radiation Research and Analysis Program under Hal Maring, NASA's Atmospheric Composition Mapping and Analysis Program under Richard Eckman, NASA's Earth Surface and Interior Program under Benjamin Phillips and the NASA Earth Observing System's Terra project. We thank James Limbacher for his assistance in the installation of the MISR 774-mixture research aerosol algorithm and his ongoing technical support.

References

Ágústsdóttir, T., Woods, J., Greenfield, T., Green, R. G., White, R. S., Winder, T., et al. (2016). Strike-slip faulting during the 2014 Bárðarbunga-Holuhraun dike intrusion, Central Iceland. *Geophysical Research Letters*, *43*, 1495–1503. https://doi.org/10.1002/2015GL067423

Arason, P., Petersen, G. N., & Bjornsson, H. (2011). Observations of the altitude of the volcanic plume during the eruption of Eyjafjallajökull, April–May 2010. *Earth System Science Data*, *3*(1), 9–17. https://doi.org/10.5194/essd-3-9-2011

Butwin, M. K., von Löwis, S., Pfeffer, M. A., & Thorsteinsson, T. (2019). The effects of volcanic eruptions on the frequency of particulate matter suspension events in Iceland. *Journal of Aerosol Science*, *128*, 99–113. https://doi.org/10.1016/j.jaerosci.2018.12.004

Carboni, E., Grainger, R. G., Mather, T. A., Pyle, D. M., Thomas, G. E., Siddans, R., et al. (2016). The vertical distribution of volcanic SO2 plumes measured by IASI. *Atmospheric Chemistry and Physics*, *16*(7), 4343–4367. https://doi.org/10.5194/acp-16-4343-2016

Carboni, E., Mather, T. A., Schmidt, A., Grainger, R. G., Pfeffer, M. A., Ialongo, I., & Theys, N. (2019). Satellite-derived sulfur dioxide (SO_2) emissions from the 2014–2015 Holuhraun eruption (Iceland). *Atmospheric Chemistry and Physics*, *19*(7), 4851–4862. https://doi.org/10.5194/acp-19-4851-2019

Carn, S. A., Clarisse, L., & Prata, A. J. (2016). Multi-decadal satellite measurements of global volcanic degassing. *Journal of Volcanology and Geothermal Research*, *311*, 99–134. https://doi.org/10.1016/j.jvolgeores.2016.01.002

Carn, S. A., Krotkov, N. A., Yang, K., & Krueger, A. J. (2013). Measuring global volcanic degassing with the ozone monitoring instrument (OMI). *Geological Society, London, Special Publications*, *380*(1), 229–257. https://doi.org/10.1144/SP380.12

Carn, S. A., Yang, K., Prata, A. J., & Krotkov, N. A. (2015). Extending the long-term record of volcanic SO_2 emissions with the ozone mapping and profiler suite nadir mapper. *Geophysical Research Letters*, *42*, 925–932. https://doi.org/10.1002/2014GL062437

Castleman, A. W. Jr., Munkelwitz, H. R., & Manowitz, B. (1974). Isotopic studies of the sulfur component of the stratospheric aerosol layer. *Tellus*, *26*(1–2), 222–234. https://doi.org/10.3402/tellusa.v26i1-2.9781

Chen, W.-T., Kahn, R. A., Nelson, D., Yau, K., & Seinfeld, J. (2008). Sensitivity of multi-angle imaging to optical and microphysical properties of biomass burning aerosols. *Journal of Geophysical Research*, *113*, D10203. https://doi.org/10.1029/2007JD009414

Cioni, R., Pistolesi, M., Bertagnini, A., Bonadonna, C., Hoskuldsson, A., & Scateni, B. (2014). Insights into the dynamics and evolution of the 2010 Eyjafjallajökull summit eruption (Iceland) provided by volcanic ash textures. *Earth and Planetary Science Letters*, *394*, 111–123. https://doi.org/10.1016/j.epsl.2014.02.051

Cooke, M. C., Francis, P. N., Millington, S., Saunders, R., & Witham, C. (2014). Detection of the Grímsvötn 2011 volcanic eruption plumes using infrared satellite measurements. *Atmospheric Science Letters*, *15*(4), 321–327. https://doi.org/10.1002/asl2.506

Dey, S., & Di Girolamo, L. (2010). A climatology of aerosol optical and microphysical properties over the Indian subcontinent from nine years (2000–2008) of multi-angle imaging Spectro Radiometer (MISR) data. *Journal of Geophysical Research*, *115*, D15204. https://doi.org/10.1029/2009JD013395

Diner, D. J., Beckert, J. C., Reilly, T. H., Bruegge, C. J., Conel, J. E., Kahn, R. A., et al. (1998). Multi-angle imaging SpectroRadiometer (MISR) instrument description and experiment overview. *IEEE Transactions on Geoscience and Remote Sensing*, *36*(4), 1072–1087. https://doi.org/10.1109/36.700992

Dubuisson, P., Herbin, H., Minvielle, F., Compiègne, M., Thieuleux, F., Parol, F., & Pelon, J. (2014). Remote sensing of volcanic ash plumes from thermal infrared: A case study analysis from SEVIRI, MODIS and IASI instruments. *Atmospheric Measurement Techniques*, *7*(2), 359–371. https://doi.org/10.5194/amt-7-359-2014

Flower, V. J., & Carn, S. A. (2015). Characterising volcanic cycles at Soufriere Hills volcano, Montserrat: Time series analysis of multi-parameter satellite data. *Journal of Volcanology and Geothermal Research*, *304*, 82–93. https://doi.org/10.1016/j.jvolgeores.2015.07.035

Flower, V. J., Carn, S. A., & Wright, R. (2016). The impact of satellite sensor viewing geometry on time-series analysis of volcanic emissions. *Remote Sensing of Environment*, *183*, 282–293. https://doi.org/10.1016/j.rse.2016.05.022

Flower, V. J., & Kahn, R. A. (2017a). Assessing the altitude and dispersion of volcanic plumes using MISR multi-angle imaging from space: Sixteen years of volcanic activity in the Kamchatka peninsula, Russia. *Journal of Volcanology and Geothermal Research*, *337*, 1–15. https://doi.org/10.1016/j.jvolgeores.2017.03.010

Flower, V. J., & Kahn, R. A. (2017b). Distinguishing remobilized ash from erupted volcanic plumes using space-borne multi-angle imaging. *Geophysical Research Letters*, *44*, 10,772–10,779. https://doi.org/10.1002/2017GL074740

Flower, V. J., & Kahn, R. A. (2020). Interpreting the volcanological processes of Kamchatka, based on multi-sensor satellite observations. *Remote Sensing of Environment*, *237*, 111585. https://doi.org/10.1016/j.rse.2019.111585

Flower, V. J. B., & Kahn, R. A. (2018). Karymsky volcano eruptive plume properties based on MISR multi-angle imagery and the volcanological implications. *Atmospheric Chemistry and Physics*, *18*(6), 3903–3918. https://doi.org/10.5194/acp-18-3903-2018

Garay, M. J., Witek, M. L., Kahn, R. A., Seidel, F. C., Limbacher, J. A., Bull, M. A., et al. (2020). Introducing the 4.4 km Spatial Resolution MISR Aerosol Products. *Atmospheric Measurement Techniques*, *13*, 593–628. https://doi.org/10.5194/amt-13-593-2020

Gíslason, S. R, Stefánsdóttir, G., Pfeffer, M. A., Barsotti, S., Jóhannsson, Th., Galeczka, I., et al. (2015). Environmental pressure from the 2014–15 eruption of Bárðarbunga volcano, Iceland. *Geochemical Perspectives Letters*, *1*, 84–93. https://doi.org/10.7185/geochemlet.1509

Gudmundsson, M. T., & Hoskuldsson, A. (2019). Eyjafjallajökull. In B. Oladottir, G. Larsen, M. T. Guðmundsson (Eds.), *Catalogue of Icelandic volcanoes*. Reykjavík: IMO, UI and CPD-NCIP. Last accessed: Jan 27, 2020. Retrieved from http://icelandicvolcanoes.is/?volcano=EYJ

Gudmundsson, M. T., & Larsen, G. (2019). Grímsvötn. In B. Oladottir, G. Larsen, M. T. Guðmundsson (Eds.), *Catalogue of Icelandic volcanoes*. Reykjavík: IMO, UI and CPD-NCIP. Last accessed: Jan 27, 2020. Retrieved from http://icelandicvolcanoes.is/?volcano=GRV

Gudmundsson, M. T., Thordarson, T., Höskuldsson, Á., Larsen, G., Björnsson, H., Prata, F. J., et al. (2012). Ash generation and distribution from the April-May 2010 eruption of Eyjafjallajökull, Iceland. *Scientific Reports*, *2*(1), 572. https://doi.org/10.1038/srep00572

Guo, Y., Tian, B., Kahn, R. A., Kalashnikova, O. V., Wong, S., & Waliser, D. E. (2013). MJO-related Atlantic dust and smoke variability in MODIS and MISR satellite observations. *Journal of Geophysical Research: Atmospheres*, *118*, 4947–4963. https://doi.org/10.1002/jgrd.50409

Hartley, M. E., Bali, E., Maclennan, J., Neave, D. A., & Halldórsson, S. A. (2018). Melt inclusion constraints on petrogenesis of the 2014–2015 Holuhraun eruption, Iceland. *Contributions to Mineralogy and Petrology*, *173*(2), 10. https://doi.org/10.1007/s00410-017-1435-0

Icelandic Meteorological Office. (2010). *Web-pages on Eyjafjallajökull eruption 2010*. Reykjavík: Icelandic Meteorological Office. Last Accessed: Jan 2020. Retrieved from https://en.vedur.is/earthquakes-and-volcanism/volcanic-eruptions/eyjafjallajokull-2010/

Icelandic Meteorological Office. (2015). *Bárðarbunga and Holuhraun—Overview*. Reykjavík: Icelandic Meteorological Office. Last Accessed: Jan 2020. Retrieved from https://en.vedur.is/earthquakes-and-volcanism/volcanic-eruptions/holuhraun/

Ilyinskaya, E., Schmidt, A., Mather, T. A., Pope, F. D., Witham, C., Baxter, P., et al. (2017). Understanding the environmental impacts of large fissure eruptions: Aerosol and gas emissions from the 2014–2015 Holuhraun eruption (Iceland). *Earth and Planetary Science Letters*, *472*, 309–322. https://doi.org/10.1016/j.epsl.2017.05.025

Johnson, B., Turnbull, K., Brown, P., Burgess, R., Dorsey, J., Baran, A. J., et al. (2012). In situ observations of volcanic ash clouds from the FAAM aircraft during the eruption of Eyjafjallajökull in 2010. *Journal of Geophysical Research*, *117*, D00U24. https://doi.org/10.1029/2011JD016760

Junghenn Noyes, K., Kahn, R., Sedlacek, A., Kleinman, L., Limbacher, J., & Li, Z. (2020). Wildfire Smoke Particle Properties and Evolution, from Space-Based Multi-Angle Imaging. *Remote Sensing*, *12*(5), 769. https://doi.org/10.3390/rs12050769

Kahn, R., Banerjee, P., & McDonald, D. (2001). The sensitivity of multiangle imaging to natural mixtures of aerosols over ocean. *Journal of Geophysical Research*, *106*(D16), 18,219–18,238. https://doi.org/10.1029/2000JD900497

Kahn, R. A., & Gaitley, B. J. (2015). An analysis of global aerosol type as retrieved by MISR. *Journal of Geophysical Research: Atmospheres*, *120*, 4248–4281. https://doi.org/10.1002/2015JD023322

Kahn, R. A., Gaitley, B. J., Garay, M. J., Diner, D. J., Eck, T., Smirnov, A., & Holben, B. N. (2010). Multiangle imaging SpectroRadiometer global aerosol product assessment by comparison with the aerosol robotic network. *Journal of Geophysical Research*, *115*, D23209. https://doi.org/10.1029/2010JD014601

Kahn, R. A., Li, W. H., Moroney, C., Diner, D. J., Martonchik, J. V., & Fishbein, E. (2007). Aerosol source plume physical characteristics from space-based multiangle imaging. *Journal of Geophysical Research*, *112*, D11205. https://doi.org/10.1029/2006JD007647

Kahn, R. A., & Limbacher, J. (2012). Eyjafjallajökull volcano plume particle-type characterization from space-based multi-angle imaging. *Atmospheric Chemistry and Physics*, *12*(20), 9459–9477. https://doi.org/10.5194/acp-12-9459-2012

Kalashnikova, O. V., & Kahn, R. A. (2006). Ability of multiangle remote sensing observations to identify and distinguish mineral dust types: Part 2. Sensitivity over dark water. *Journal of Geophysical Research*, *111*, D11207. https://doi.org/10.1029/2005JD006756

Kalashnikova, O. V., & Kahn, R. A. (2008). Mineral dust plume evolution over the Atlantic from combined MISR/MODIS aerosol retrievals. *Journal of Geophysical Research*, *113*, D24204. https://doi.org/10.1029/2008JD010083

Kalashnikova, O. V., Kahn, R., Sokolik, I. N., & Li, W.-H. (2005). Ability of multiangle remote sensing observations to identify and distinguish mineral dust types: Optical models and retrievals of optically thick plumes. *Journal of Geophysical Research*, *110*, D18S14. https://doi.org/10.1029/2004JD004550

Kalnay, E., Kanamitsu, M., Kistler, R., Collins, W., Deaven, D., Gandin, L., et al. (1996). The NCEP/NCAR 40-year reanalysis project. *Bulletin of the American Meteorological Society*, *77*(3), 437–471. https://doi.org/10.1175/1520-0477(1996)077<0437:TNYRP>2.0.CO;2

Kaufman, Y. J., Justice, C. O., Flynn, L. P., Kendall, J. D., Prins, E. M., Giglio, L., et al. (1998). Potential global fire monitoring from EOS-MODIS. *Journal of Geophysical Research*, *103*, 32215–32238. https://doi.org/10.1029/98JD01644

Krotkov, N. A., Carn, S. A., Krueger, A. J., Bhartia, P. K., & Yang, K. (2006). Band residual difference algorithm for retrieval of SO_2 from the Aura ozone monitoring instrument (OMI). *Geoscience and Remote Sensing, IEEE Transactions on*, *44*(5), 1259–1266. https://doi.org/10.1109/TGRS.2005.861932

Krueger, A. J. (1983). Sighting of El Chichon sulfur dioxide clouds with the Nimbus 7 total ozone mapping spectrometer. *Science*, *220*(4604), 1377–1379. https://doi.org/10.1126/science.220.4604.1377

Lacis, A., Hansen, J., & Sato, M. (1992). Climate forcing by stratospheric aerosols. *Geophysical Research Letters*, *19*(15), 1607–1610. https://doi.org/10.1029/92GL01620

Laeger, K., Petrelli, M., Andronico, D., Misiti, V., Scarlato, P., Cimarelli, C., et al. (2017). High-resolution geochemistry of volcanic ash highlights complex magma dynamics during the Eyjafjallajökull 2010 eruption American Mineralogist. *Journal of Earth and Planetary Materials*, *102*(6), 1173–1186. https://doi.org/10.2138/am-2017-5860

Larsen, G., & Gudmundsson, M. T. (2019). Bárðarbunga. In B. Oladottir, G. Larsen, M. T. Guðmundsson (Eds.), *Catalogue of Icelandic volcanoes*. Reykjavík: IMO, UI and CPD-NCIP. Last accessed: Jan 27, 2020. Retrieved from http://icelandicvolcanoes.is/?volcano=BAR

Limbacher, J. A., & Kahn, R. A. (2014). MISR research-aerosol-algorithm: Refinements for dark water retrievals. *Atmospheric Measurement Techniques*, *7*(1), 1–12. https://doi.org/10.5194/amt-7-1-2014

Limbacher, J. A., & Kahn, R. A. (2017). Updated MISR dark water research aerosol retrieval algorithm—Coupled 1.1 km ocean surface chlorophyll-a retrievals with empirical calibration corrections. *Atmospheric Measurement Techniques*, *10*(4), 1539–1555. https://doi.org/10.5194/amt-10-1539-2017

Liu, E. J., Cashman, K. V., Beckett, F. M., Witham, C. S., Leadbetter, S. J., Hort, M. C., & Guðmundsson, S. (2014). Ash mists and brown snow: Remobilization of volcanic ash from recent Icelandic eruptions. *Journal of Geophysical Research: Atmospheres*, *119*, 9463–9480. https://doi.org/10.1002/2014JD021598

Lyons, J. J., Waite, G. P., Rose, W. I., & Chigna, G. (2010). Patterns in open vent, Strombolian behavior at Fuego volcano, Guatemala, 2005–2007. *Bulletin of Volcanology*, *72*(1), 1–15. https://doi.org/10.1007/s00445-009-0305-7

Malavelle, F. F., Haywood, J. M., Jones, A., Gettelman, A., Clarisse, L., Bauduin, S., et al. (2017). Strong constraints on aerosol–cloud interactions from volcanic eruptions. *Nature*, *546*(7659), 485–491. https://doi.org/10.1038/nature22974

Martonchik, J. V., Diner, D. J., Crean, K. A., & Bull, M. A. (2002). Regional aerosol retrieval results from MISR. *IEEE Transactions on Geoscience and Remote Sensing*, *40*(7), 1520–1531. https://doi.org/10.1109/TGRS.2002.801142

Martonchik, J. V., Kahn, R. A., & Diner, D. J. (2009). Retrieval of aerosol properties over land using MISR observations. In A. Kokhanovsky (Ed.), *Satellite aerosol remote sensing over land* (pp. 267–291). Berlin: Springer. https://doi.org/10.1007/978-3-540-69397-0_9

McCormick, B. T., Edmonds, M., Mather, T. A., Campion, R., Hayer, C. S., Thomas, H. E., & Carn, S. A. (2013). Volcano monitoring applications of the ozone monitoring instrument. *Geological Society, London, Special Publications*, *380*(1), 259–291. https://doi.org/10.1144/SP380.11

McCormick Kilbride, B. T., Mulina, K., Wadge, G., Johnson, R., Itikarai, I., & Edmonds, M. (2019). Multi-year satellite observations of sulfur dioxide gas emissions and lava extrusion at Bagana Volcano Papua New Guinea. *Frontiers in Earth Science*, *7*. https://doi.org/10.3389/feart.2019.00009

Moroney, C., Davies, R., & Muller, J. P. (2002). Operational retrieval of cloud-top heights using MISR data. *IEEE Transactions on Geoscience and Remote Sensing*, *40*(7), 1532–1540. https://doi.org/10.1109/TGRS.2002.801150

Moxnes, E. D., Kristiansen, N. I., Stohl, A., Clarisse, L., Durant, A., Weber, K., & Vogel, A. (2014). Separation of ash and sulfur dioxide during the 2011 Grímsvötn eruption. *Journal of Geophysical Research: Atmospheres*, *119*, 7477–7501. https://doi.org/10.1002/2013JD021129

Muller, J. P., Mandanayake, A., Moroney, C., Davies, R., Diner, D. J., & Paradise, S. (2002). MISR stereoscopic image matchers: Techniques and results. *IEEE Transactions on Geoscience and Remote Sensing*, *40*(7), 1547–1559. https://doi.org/10.1109/TGRS.2002.801160

Murphy, S. W., Wright, R., Oppenheimer, C., & Souza Filho, C. R. (2013). MODIS and ASTER synergy for characterizing thermal volcanic activity. *Remote Sensing of Environment*, *131*, 195–205. https://doi.org/10.1016/j.rse.2012.12.005

Nelson, D. L., Chen, Y., Kahn, R. A., Diner, D. J., & Mazzoni, D. (2008). Example applications of the MISR INteractive eXplorer (MINX) software tool to wildfire smoke plume analyses. *Proc. SPIE*, *7089*(09), 1–11. https://doi.org/10.1117/12.795087

Nelson, D. L., Garay, M. J., Kahn, R. A., & Dunst, B. A. (2013). Stereoscopic height and wind retrievals for aerosol plumes with the MISR INteractive eXplorer (MINX). *Remote Sensing*, *5*(9), 4593–4628. https://doi.org/10.3390/rs5094593

Newhall, C. G., & Self, S. (1982). The volcanic explosivity index (VEI) an estimate of explosive magnitude for historical volcanism. *Journal of Geophysical Research*, *87*(C2), 1231–1238. https://doi.org/10.1029/JC087iC02p01231

Pavolonis, M. J., Heidinger, A. K., & Sieglaff, J. (2013). Automated retrievals of volcanic ash and dust cloud properties from upwelling infrared measurements. *Journal of Geophysical Research: Atmospheres*, *118*, 1436–1458. https://doi.org/10.1002/jgrd.50173

Pedersen, G. B. M., Höskuldsson, A., Dürig, T., Thordarson, T., Jonsdottir, I., Riishuus, M. S., et al. (2017). Lava field evolution and emplacement dynamics of the 2014–2015 basaltic fissure eruption at Holuhraun, Iceland. *Journal of Volcanology and Geothermal Research*, *340*, 155–169. https://doi.org/10.1016/j.jvolgeores.2017.02.027

Petersen, G. N., Bjornsson, H., Arason, P., & Löwis, S. V. (2012). Two weather radar time series of the altitude of the volcanic plume during the May 2011 eruption of Grímsvötn, Iceland. *Earth System Science Data*, *4*(1), 121–127. https://doi.org/10.5194/essd-4-121-2012

Pfeffer, M. A., Bergsson, B., Barsotti, S., Stefánsdóttir, G., Galle, B., Arellano, S., et al. (2018). Ground-based measurements of the 2014–2015 Holuhraun volcanic cloud (Iceland). *Geosciences*, *8*(1), 29. https://doi.org/10.3390/geosciences8010029

Pollack, J. B., Toon, O. B., Sagan, C., Summers, A., Baldwin, B., & Van Camp, W. (1976). Volcanic explosions and climatic change: A theoretical assessment. *Journal of Geophysical Research*, *81*(6), 1071–1083. https://doi.org/10.1029/JC081i006p01071

Prata, F., Woodhouse, M., Huppert, H. E., Prata, A., Thordarson, T., & Carn, S. (2017). Atmospheric processes affecting the separation of volcanic ash and SO_2 in volcanic eruptions: Inferences from the May 2011 Grímsvötn eruption. *Atmospheric Chemistry and Physics*, *17*(17), 10,709–10,732. https://doi.org/10.5194/acp-17-10709-2017

Salomonson, V. V., Barnes, W. L., Maymon, P. W., Montgomery, H. E., & Ostrow, H. (1989). MODIS: Advanced facility instrument for studies of the earth as a system. *IEEE Transactions on Geoscience and Remote Sensing*, *27*(2), 145–153. https://doi.org/10.1109/36.20292

Schumann, U., Weinzierl, B., Reitebuch, O., Schlager, H., Minikin, A., Forster, C., et al. (2011). Airborne observations of the Eyjafjalla volcano ash cloud over Europe during air space closure in April and May 2010. *Atmospheric Chemistry and Physics*, *11*(5), 2245–2279. https://doi.org/10.5194/acp-11-2245-2011

Scollo, S., Folch, A., Coltelli, M., & Realmuto, V. J. (2010). Three-dimensional volcanic aerosol dispersal: A comparison between multiangle imaging Spectroradiometer (MISR) data and numerical simulations. *Journal of Geophysical Research*, *115*, D24210. https://doi.org/10.1029/2009JD013162

Scollo, S., Kahn, R. A., Nelson, D. L., Coltelli, M., Diner, D. J., Garay, M. J., & Realmuto, V. J. (2012). MISR observations of Etna volcanic plumes. *Journal of Geophysical Research*, *117*, D06210. https://doi.org/10.1029/2011JD016625

Sigmarsson, O., Vlastelic, I., Andreasen, R., Bindeman, I., Devidal, J. L., Moune, S., et al. (2011). Remobilization of silicic intrusion by mafic magmas during the 2010 Eyjafjallajökull eruption. *Solid Earth*, *2*(2), 271–281. https://doi.org/10.5194/se-2-271-2011

Sigmundsson, F., Hreinsdóttir, S., Hooper, A., Árnadóttir, T., Pedersen, R., Roberts, M. J., et al. (2010). Intrusion triggering of the 2010 Eyjafjallajökull explosive eruption. *Nature*, *468*(7322), 426–430. https://doi.org/10.1038/nature09558

Sigurdsson, H., Houghton, B., McNutt, S., Rymer, H., & Stix, J. (Eds.) (2015). *The encyclopedia of volcanoes* (2nd ed.). London: Elsevier. ISBN: 978-0123859389

Simmons, I. C., Pfeffer, M. A., Calder, E. S., Galle, B., Arellano, S., Coppola, D., & Barsotti, S. (2017). Extended SO 2 outgassing from the 2014–2015 Holuhraun lava flow field, Iceland. *Bulletin of Volcanology*, *79*(11), 79. https://doi.org/10.1007/s00445-017-1160-6

Sparks, R. S. J., Bursik, M. I., Carey, S. N., Gilbert, J., Glaze, L. S., Sigurdsson, H., & Woods, A. W. (1997). *Volcanic plumes*. Chichester: Wiley. ISBN: 0471939013

Stefánsson, A., Stefánsdóttir, G., Keller, N. S., Barsotti, S., Sigurdsson, Á., Thorláksdóttir, S. B., et al. (2017). Major impact of volcanic gases on the chemical composition of precipitation in Iceland during the 2014–2015 Holuhraun eruption. *Journal of Geophysical Research: Atmospheres*, *122*, 1971–1982. https://doi.org/10.1002/2015JD024093

Stohl, A., Prata, A. J., Eckhardt, S., Clarisse, L., Durant, A., Henne, S., et al. (2011). Determination of time-and height-resolved volcanic ash emissions and their use for quantitative ash dispersion modeling: The 2010 Eyjafjallajökull eruption. *Atmospheric Chemistry and Physics*, *11*(9), 4333–4351. https://doi.org/10.5194/acp-11-4333-2011

Thomas, H. E., & Prata, A. J. (2011). Sulphur dioxide as a volcanic ash proxy during the April–May 2010 eruption of Eyjafjallajökull volcano. *Iceland Atmospheric Chemistry and Physics*, *11*(14), 6871–6880. https://doi.org/10.5194/acp-11-6871-2011

Torres, O., Bhartia, P. K., Jethva, H., & Ahn, C. (2018). Impact of the ozone monitoring instrument row anomaly on the long-term record of aerosol products. *Atmospheric Measurement Techniques*, *11*(5), 2701–2715. https://doi.org/10.5194/amt-11-2701-2018

Turnbull, K., Johnson, B., Marenco, F., Haywood, J., Minikin, A., Weinzierl, B., et al. (2012). A case study of observations of volcanic ash from the Eyjafjallajökull eruption: 1 In situ airborne observations. *Journal of Geophysical Research*, *117*, D00U12. https://doi.org/10.1029/2011JD016688

Val Martin, M., Logan, J. A., Kahn, R. A., Leung, F.-Y., Nelson, D., & Diner, D. (2010). Fire smoke injection heights over North America constrained from the Terra multi-angle imaging SpectroRadiometer. *Atmospheric Chemistry and Physics*, *10*(4), 1491–1510. https://doi.org/10.5194/ACP-10-1491-2010

Vignelles, D., Roberts, T. J., Carboni, E., Ilyinskaya, E., Pfeffer, M., Waldhauserova, P. D., et al. (2016). Balloon-borne measurement of the aerosol size distribution from an Icelandic flood basalt eruption. *Earth and Planetary Science Letters*, *453*, 252–259. https://doi.org/10.1016/j.epsl.2016.08.027

Watson, I. M., Realmuto, V. J., Rose, W. I., Prata, A. J., Bluth, G. J., Gu, Y., et al. (2004). Thermal infrared remote sensing of volcanic emissions using the moderate resolution imaging spectroradiometer. *Journal of Volcanology and Geothermal Research*, *135*(1–2), 75–89. https://doi.org/10.1016/j.jvolgeores.2003.12.017

Winker, D. M., Liu, Z., Omar, A., Tackett, J., & Fairlie, D. (2012). CALIOP observations of the transport of ash from the Eyjafjallajökull volcano in April 2010. *Journal of Geophysical Research*, *117*, D00U15. https://doi.org/10.1029/2011JD016499

Wright, R. (2016). MODVOLC: 14 years of autonomous observations of effusive volcanism from space. *Geological Society, London, Special Publications*, *426*(1), 23–53. https://doi.org/10.1144/SP426.12

Wright, R., Flynn, L., Garbeil, H., Harris, A., & Pilger, E. (2002). Automated volcanic eruption detection using MODIS. *Remote Sensing of Environment*, *82*(1), 135–155. https://doi.org/10.1016/S0034-4257(02)00030-5

Wright, R., Flynn, L. P., Garbeil, H., Harris, A. J., & Pilger, E. (2004). MODVOLC: Near-real-time thermal monitoring of global volcanism. *Journal of Volcanology and Geothermal Research*, *135*(1–2), 29–49. https://doi.org/10.1016/j.jvolgeores.2003.12.008